



**HAL**  
open science

## **A creeping intracontinental thrust fault: past and present slip-rates on the Northern edge of the Tien Shan, Kazakhstan**

D Mackenzie, Richard Walker, Kanatbek Abdrakhmatov, Grace Campbell, Andrew Carr, Christoph Gruetzner, Aidyn Mukambayev, Magali Rizza

### ► To cite this version:

D Mackenzie, Richard Walker, Kanatbek Abdrakhmatov, Grace Campbell, Andrew Carr, et al.. A creeping intracontinental thrust fault: past and present slip-rates on the Northern edge of the Tien Shan, Kazakhstan. *Geophysical Journal International*, 2018, 215 (2), pp.1148-1170. 10.1093/gji/ggy339 . hal-02115894

**HAL Id: hal-02115894**

**<https://hal.science/hal-02115894>**

Submitted on 30 Apr 2019

**HAL** is a multi-disciplinary open access archive for the deposit and dissemination of scientific research documents, whether they are published or not. The documents may come from teaching and research institutions in France or abroad, or from public or private research centers.

L'archive ouverte pluridisciplinaire **HAL**, est destinée au dépôt et à la diffusion de documents scientifiques de niveau recherche, publiés ou non, émanant des établissements d'enseignement et de recherche français ou étrangers, des laboratoires publics ou privés.



Distributed under a Creative Commons Attribution 4.0 International License

1 **A Creeping Intracontinental Thrust Fault: Past and**  
2 **Present Slip-Rates on the Northern Edge of the Tien**  
3 **Shan, Kazakhstan**

4 D. Mackenzie<sup>1,9</sup>, Richard Walker<sup>1\*</sup>, Kanatbek Abdrakhmatov<sup>2</sup>,  
5 Grace Campbell<sup>3,4</sup>, Andrew Carr<sup>5</sup>, Christoph Gruetzner<sup>3,6</sup>,  
6 Aidyn Mukambayev<sup>7</sup>, Magali Rizza<sup>8</sup>

<sup>1</sup> *COMET, Dept. of Earth Sciences, University of Oxford, Oxford, OX1 3AN, UK.*

<sup>2</sup> *Institute of Seismology, National Academy of Sciences, Kyrgyz Republic.*

<sup>3</sup> *COMET, Bullard Laboratories, Cambridge University, Madingley Road, Cambridge,  
CB3 0EZ, UK.*

<sup>4</sup> *Now at Arup, 13 Fitzroy St, London, Middlesex W1T 4BQ, UK.*

<sup>5</sup> *School of Geography, Geology and the Environment, University of Leicester, University Road, Leicester  
LE1 7RH, UK.*

<sup>6</sup> *Now at Friedrich-Schiller-Universität Jena, Institut für Geowissenschaften,  
Burgweg 11, 07749 Jena, Germany.*

<sup>7</sup> *Data Center of the Institute of Geophysical Researches, L. Chaikinoy Street 4,  
Almaty 050020, Kazakhstan.*

<sup>8</sup> *Aix Marseille Univ, CNRS, IRD, INRA, Coll France, CEREGE, Aix-en-Provence, France*

<sup>9</sup> *Now at 3vGeomatics, Vancouver, BC, V5Y 1K6, Canada*

8 **SUMMARY**

9  
10 We demonstrate that a continental interior reverse fault is deforming by aseismic creep,  
11 presently, and likely also in the long term. The Karkara Rangefront Fault, part of the  
12 larger Main Terskey Front, forms the northern boundary of the high Terskey Tien Shan  
13 in southeastern Kazakhstan and is a mature structure with evidence for high slip rates  
14 throughout the late Cenozoic. Combining field studies with a satellite stereo-image de-  
15 rived digital elevation model (2 m resolution), we map a series of fluvial terraces along the  
16 rangefront which are uplifted by up to  $\sim 300$  m above the present river level. Radiocarbon  
17 ages from one catchment constrain the ages of the lowermost two terraces to be  $\sim 4$ – $5$  ka  
18 and  $\sim 10$ – $15$  ka, consistent with prominent, regionally extensive terraces observed else-  
19 where in the Tien Shan. Based on conservative estimates for the fault dip under the  
20 displaced terraces, we estimate a slip rate along the fault plane of  $3.5_{-0.4}^{+1.7}$  mm/yr on the  
21 Karkara Rangefront Fault and a further  $>0.8$  mm/yr on a fold structure in the Kegen  
22 basin that we infer is driven by a detachment from the main rangefront. We therefore  
23 estimate a minimum shortening rate across the rangefront of 1.1–3.3 mm/yr. Elastic  
24 modelling of the regional GPS velocity field suggests that the fault is presently creep-  
25 ing at  $\sim 3$  mm/yr (horizontal shortening), consistent with the upper limit of our Late  
26 Quaternary slip rate estimate. This is the fastest known slip rate in the northern Tien  
27 Shan and the only individual structure resolved in the regional velocity field. At present  
28 the fault is accumulating minimal strain, and there is evidence in the geomorphology  
29 that this creep is sustained in the long term, but whether or not it is also capable of  
30 generating earthquakes requires further study.

31 **Key words:** Seismic Cycle – Continental tectonics: compressional – Crustal structure  
32 – Geomorphology – Aseismic Creep

\* Correspondence to: richard.walker@earth.ox.ac.uk

## 1 INTRODUCTION

The classical model of earthquakes and faulting in the continents is that of stick-slip behaviour on discrete faults. This model is characterised by three main parts: interseismic strain accumulation, coseismic release and postseismic relaxation (e.g. Reid 1910; Smith & Wyss 1968; Thatcher 1983). More recently however, a subset of faults, generally major continental strike-slip faults, have been observed to deform by a different mode - that of aseismic creep, either at steady rates or in shorter bursts, which accommodates some fraction of the long-term fault motion. The interactions between creeping and non-creeping segments of faults and the mechanisms by which they creep are the subject of much discussion (e.g. Avouac 2015; Harris 2017) and the seismic hazard that creeping faults pose is not well understood (Chen & Bürgmann 2017). Case studies of creeping continental faults have generally been conducted on large strike-slip faults at or near plate margins. By comparison fault slip rates in the more slowly deforming continental interiors are often too low and instrumentation too sparse to resolve creep.

Here, we present a case study of the northern rangefront fault of the high Tien Shan, adjacent to the highest peaks of the range, where creep on a continental interior thrust fault is suspected (Figure 1). The regional GPS velocity field shows that the Tien Shan accommodate  $\sim 20 \pm 2$  mm/yr of shortening (at the longitude of this study), amounting to around half the total India–Eurasia plate convergence (Tapponnier & Molnar 1979; Abdrakhmatov et al. 1996; Zubovich et al. 2010). Approximately half of this shortening,  $\sim 10$  mm/yr, is taken up across the northern and central Tien Shan, with the other half accommodated along the northern margin of the Tarim Basin. The majority of faults are not resolved in the regional GPS velocity field, which shows a remarkably linear velocity ramp right across the Tien Shan (England & Molnar 2015). The only exception is a discrete step in the velocity field, extending from Song-Kul lake in Kyrgyzstan at least as far as the Kegen Basin, roughly paralleling the Terskey Range (Figure 1). The velocity field of Zubovich et al. (2010) only extends as far as the Kazakh-Chinese border, so it is possible that the step extends eastwards into China but is unresolved. England & Molnar (2015) suggest that this step is probably

61 due to a creeping or very shallowly locked fault. At the Kegen basin, this step is a 3-4 mm/yr  
62 drop in northwards velocity, the location of which coincides very closely with the northern  
63 rangefront of the Terskey Tien Shan (Figure 1).

64 Faults are mapped along the 500 km length of the northern rangefront of the Terskey  
65 range (Tapponnier & Molnar 1979; Delvaux et al. 2001; Deng et al. 2003, 2004; Macaulay  
66 et al. 2013; Campbell et al. 2013), but there are no published slip-rate studies or geomor-  
67 phological observations. We present detailed forensic investigation of the range-front faults  
68 adjacent to the Kegen basin of Kazakhstan, where flights of well preserved river terraces  
69 record fault displacement through the late Quaternary and the regional GPS velocity field is  
70 relatively dense. Our analysis centres on the main rangefront fault (the Karkara Rangefront,  
71 KRF), and also a foreland fold structure (the Kegen Basin Fold, KBF) that runs through  
72 the middle of the Kegen Basin (Figure 1b), and which is likely to be linked to the rangefront  
73 fault at depth. Important steps in our analysis are to establish long-term rates of shortening  
74 for comparison to those derived from GPS, and also to examine the geomorphology for indi-  
75 cations of long-term sustained creep at the surface. We then fit an elastic dislocation model  
76 to the GPS data, demonstrating a rapid creep rate across the fault at the present day, and  
77 then compare the observed present-day creep rate to our estimate of late Quaternary slip  
78 rate, assessing the capacity of this fault to produce large earthquakes.

79 We are aided in our study of the geology and geomorphology by the use high resolution  
80 digital elevation models (DEMs) derived from 0.7 m resolution stereo Pléiades satellite im-  
81 agery and from low-altitude aerial survey. Full details of the DEM construction methods,  
82 and of the quaternary dating techniques that we use, are provided as supplementary infor-  
83 mation, and included in the main text where appropriate. All quaternary dating results are  
84 provided in the main text as tables.

## 85 **2 QUATERNARY SLIP ON THE KARKARA RANGEFRONT**

86 The KRF strikes approximately E-W and dips to the south, forming the southern boundary  
87 of the Kegen Basin (Figure 1). At the western end, the fault splits into several strands, one

88 following a fold structure to the edge of lake Issyk Kul (and likely underneath, Gebhardt  
89 et al. 2017), while the other follows the main rangefront of the high topography south of the  
90 lake (MTF, Figure 1b). The hangingwall range is cored with Palaeozoic basement, but the  
91 surface expression of the KRF has propagated 2-3 km north from the Palaeozoic contact,  
92 and Neogene basin deposits are uplifted in the immediate hangingwall. We measure the  
93 present day shape of the terraces to estimate the underlying fault structure and the uplift  
94 and hence fault slip since abandonment (e.g. Thompson et al. 2002; Burbank & Anderson  
95 2011).

96 The river terraces are cut into Neogene sediments and generally capped with fluvial  
97 gravels, followed by a post-abandonment soil development. Unfortunately, the Neogene de-  
98 posits are poorly exposed and heavily eroded so we were unable to estimate bedding plane  
99 orientations in any of the river catchments. At three river valleys crossing the fault, we  
100 map prominent flights of terraces (catchments Rc1–3, Figures 1b, 2b). At the eastern end  
101 (Rc1), the fault trace reaches the surface  $\sim 2$  km from the Palaeozoic–Cenozoic contact, but  
102 the contact strikes SW while the fault continues E-W, giving a separation of  $\sim 15$  km at  
103 catchment Rc3, suggesting lateral changes in segmentation or in the shallow fault geometry  
104 (Figure 2).

105 At Rc1 we used the field observations, SfM and satellite DEMs to map the fluvial terraces  
106 at high resolution. We then extended the terrace mapping along the rangefront to using the  
107 satellite derived DEM to cover a much larger area than is practical in the field. Several  
108 additional catchments Rc4–6 are also covered by the DEM, but they are much smaller than  
109 Rc1–3 so the terraces are shorter and fewer are preserved. Mapping and terrace profiles for  
110 Rc4–6 are given in Supplement S2. In all six catchments we identify at least three well defined  
111 terraces, one of which is uplifted by  $\sim 15$ – $20$  m in each case and shows similar degrees of  
112 post-abandonment incision – we suggest that this surface may correspond to the widespread  
113 Q(3)III surface identified by Thompson et al. (2002).

## 2.1 Results: River Catchment 1 (Rc1), High resolution survey

At the eastern end of the Karkara fault section, we chose a river valley site with a well developed flight of terraces (Figure 3a-c) as the case study for high-resolution surveying with SfM (Figure 3d). In its upper catchment, the river runs S to N in a deeply incised valley in the Palaeozoic bedrock, before crossing into Cenozoic deposits  $\sim 2$  km from the main fault trace. Where exposed, the Neogene sediments are homogeneous fine grained, dark red in colour, with a clay-like consistency and show little stratigraphy. The poorly consolidated material and generally only thin gravel cap on the terraces, has not preserved fault plane exposures. Landsliding has also occurred in the sediments in several locations along the range front (Figure 3b,c), obscuring the terrace levels.

### 2.1.1 Rc1: Terrace offsets

Using the combined elevation datasets, we map four discrete major terrace levels at Rc1 (T1–4), of which three are preserved on both sides of the river (Figure 3b-d). A kinematic GPS profile along the river base was used to constrain the present-day longitudinal river profile as this provides a better constraint on the river elevation than the photogrammetry DEMs, which decorrelate on water. We determine the elevations of each terrace above the current footwall surface and the river level. Figure 4 shows profiles of each terrace with a constant river gradient removed (estimated from the approximately linear stretch of the river profile  $< 1600$  m upstream from the fault).

The most recent major terrace (labelled T1) is observed as a pair of well preserved surfaces on both sides of the present river channel, though only the western side is preserved at the fault trace. The surface is generally planar and parallel to the river bed, with the exception of two sections,  $\sim 100$ - $220$  m and  $\sim 750$ - $900$  m from the fault surface trace (Figure 4), which have been tilted to the south, and which we attribute to step changes in fault dip below these regions (e.g. Le Béon et al. 2014). We measure the displacement of the T1 surface since abandonment relative to the downthrown fan surface as  $12.9 \pm 0.5$  m in the

140 immediate 50-100 m of the hangingwall, reducing to  $10.0 \pm 0.5$  m  $\sim 200$  m from the scarp  
 141 (Figure 4).

142 The second terrace (labelled T2, Figures 3) is also preserved on both sides of the river,  
 143 though only a small remnant exists on the eastern side around  $\sim 1.3$  km upstream from the  
 144 fault. The T2 surface also has two sections that are apparently tilted southwards, one at  
 145 800–900 m from the fault with a gentle slope of  $\sim 1.5^\circ$ S and a second in the 100-200 m closest  
 146 to the fault, with a slope of  $\sim 4^\circ$ S. These two sections are coincident with the southward-  
 147 tilted sections of T1. Near the fault, the T2 surface is  $\sim 36.3 \pm 1.7$  m above the current river  
 148 level (Figure 4). However, projecting the river-parallel part of the terrace gradient to the  
 149 current fault trace suggests the terrace is  $\sim 21.8 \pm 1.4$  m above the present river level at the  
 150 fault. The different degree of uplift on each section of the terrace surface is likely to be due  
 151 to changes in the fault dip, with a steeper dip under the section nearest the fault trace. We  
 152 note that the fan aggradation during T1 formation will have buried the footwall remnant of  
 153 T2, so the observed uplift is a minimum since abandonment.

154 T3 is mainly preserved on the eastern bank, though there is a small remnant on the  
 155 western side (Figures 3–4). The terrace is not preserved in the vicinity of the fault scarp,  
 156 so estimating the total displacement requires significant extrapolation giving large associ-  
 157 ated errors. At the location of our sample (A3, Figure 3d), the eastern and western terrace  
 158 remnants are at heights of  $\sim 42$  m and  $\sim 35$  m above the modern footwall surface respec-  
 159 tively; we attribute this difference to the asymmetry of the drainage and the river not being  
 160 perpendicular to the fault, but they may also be two separate sub-terraces. Projecting the  
 161 gradient of the terrace to the present fault surface trace, we estimate a minimum uplift of  
 162  $45 \pm 5$  m since abandonment for the larger remnant.

163 Only a small remnant of T4 exists at a significant distance from the surface trace so  
 164 the uplift is poorly constrained. Scaling the T1 profile up to T4, we estimate a minimum  
 165 displacement of  $53 \pm 5$  m. There are several locations where subsidiary terraces were also  
 166 noted, but as they have minimal extent we do not analyse them further.

167 In addition to the deformation of the terrace surfaces, we also note a deflection of the

168 river gradient. The river shows a short wavelength step of  $\sim 2.5 \pm 0.5$  m (significant against  
169 the noise level, Figure 4), which has not migrated upstream significantly from the fault.  
170 There is no bedrock visible in the modern stream bed and the Neogene sediments are very  
171 soft and unlikely to generate a material contrast strong enough to cause this deflection purely  
172 due to a change in lithology. It is likely therefore that this deflection arises from motion on  
173 the fault, though given the relatively diffuse nature of the deflection, it is not possible to  
174 distinguish whether it has been generated by continuous creep, a palaeoearthquake, or a  
175 combination of both mechanisms.

### 176 *2.1.2 Terrace Deformation*

177 Approximately 200 m south of the scarp, T1 shows a kink in height by  $1.7 \pm 0.3$  m over a  
178 distance of  $\sim 70$  m. At the corresponding point in T2, the remainder of the terrace south  
179 of the kink changes gradient from approximately river parallel to  $4.5^\circ$  relative to the river  
180 gradient, dipping to the south (away from the fault trace). We attribute this feature to a  
181 steepening of the fault dip towards the surface in the uppermost 50–100 m of sediments.  
182 This step preserved in both terraces closely resembles fold scarps generated by fault-bend  
183 folding (e.g. Le Béon et al. 2014). The step has resulted in a distinctive short wavelength  
184 ( $\sim 100$  m) raised topographic feature in the immediate hangingwall of the fault along much  
185 of the range front (Figure 2b), though it has been eroded in places by landsliding of the soft  
186 Neogene sediments.

187 Further into the hangingwall, we noted a second back-tilted section in both T1 and T2,  
188 which we again attribute to a steepening of the fault under this section ( $\sim 800$  m from the  
189 fault trace). Under this model, we would expect the ratio of the step offset in T1 to the  
190 step offset in T2 to equal the ratio of total fault slip since abandonment of each terrace.  
191 Significant noise due to erosion of the terrace surface gives large errors, but we estimate  
192 a ratio of  $1.9 \pm 0.4$  i.e. T2 records approximately twice as much slip as T1 (Figure 4). For  
193 comparison, we estimate the ratio of the elevation of the terrace surfaces relative to modern  
194 river level either side of the fold scarp giving  $2.16 \pm 0.09$  (north) and  $2.25 \pm 0.15$  (south), the

195 same as the ratio of slip estimated from the fold scarps (within error). This suggests that  
 196 the elevation of the T2 terrace above present river level is a good measure of the total uplift  
 197 of T2 since abandonment (within error), so there may have been only minimal burial of this  
 198 surface in the footwall (<20% of the uplift).

### 199 2.1.3 Rc1: Terrace Chronology

200 We excavated a pit into each terrace surface, choosing locations to minimise the likelihood  
 201 of post abandonment deposition or erosion i.e. well away from up-slope risers or stream  
 202 channels (locations A1–A4 in Figure 3d). We also sampled from a stream cut exposure in  
 203 the footwall surface (A0). Though attempts were made to measure quartz OSL (optically-  
 204 stimulated luminescence) and feldspar IRSL (infra-red stimulated luminescence) ages from  
 205 the luminescence samples (OSL1 and OSL2 from A0 and A1), the sample material proved  
 206 unreliable for both methods in both samples. Quartz measurements showed very dim signals  
 207 lacking a rapidly bleaching “fast” component. Feldspar measurements were brighter, but  
 208 showed larger inter-aliquot spread and large residuals after bleaching, suggesting incomplete  
 209 bleaching prior to deposition – ages are shown in Table 1, but the interpretation is unclear.  
 210 We therefore discuss only radiocarbon ages from this catchment. As there was no discrete  
 211 identifiable organic matter available, we were restricted to bulk dating of organic rich sed-  
 212 iment samples from within the terrace deposits – generally, dark consolidated palaeo-soil  
 213 clasts were used (Table 1).

214 In the footwall, a river cut exposes the uppermost stratigraphy which consists of a soil  
 215 cap of ~40 cm overlying angular gravels (up to ~15 cm diameter) with occasional coarse  
 216 sand lenses Figure 5. However only the uppermost 2 m is exposed, so the depth of the  
 217 Neogene contact in the footwall is unknown.

218 The terrace surface of T1 in the hangingwall consists of a ~35 cm soil cap on top of  
 219 gravels, which were estimated to be ~2–4 m thick, lying unconformably on top of the red  
 220 Neogene sediments (observed in river cuttings, Figure 5). Given the similar gravel cap in the  
 221 footwall and hangingwall, it is likely that the surface in the footwall represents the correlated

222 T1 surface. Our only successful age constraint comes from radiocarbon bulk samples, which  
223 provide estimates of the pre and post abandonment ages. Sample C3 from the base of the  
224 soil layer (depth  $\sim 35\text{--}41$  cm, Figure 5) at A1 was a very dark organic rich soil layer, which  
225 yielded a calibrated age of 4.0–4.2 ka BP. Thompson et al. (2002) suggest that samples  
226 from the base of the post-abandonment deposits generally give a tight post-date on terrace  
227 abandonment. Sample C4 from a depth of  $\sim 58$  cm at A0 was a  $\sim 6$  cm soil clast embedded  
228 within the gravel matrix, which yielded a calibrated age of 9.6–9.7 ka BP, a pre-date on  
229 terrace abandonment. As these gravels cover the footwall remnant of T2, this must also  
230 post-date the abandonment of T2.

231 T2 consists of a thicker soil development of  $\sim 60$  cm overlying red clay, with a poorly  
232 defined interface. The red clay contains occasional gravels ( $< 10$  cm). Given the thick soil  
233 development on the T1 terrace, a significant proportion of the soil development on this  
234 terrace is likely to post-date T1 too. Sample C5 (pit A2), a consolidated organic rich soil  
235 clast treated as a bulk sediment sample was extracted from within the mixed gravel and  
236 clays at a depth of  $\sim 124$  cm and yielded a calibrated age of 14.2–14.9 ka BP. Given that  
237 this sample was within the upper part of the pre-abandonment deposits, it suggests that the  
238 terrace was abandoned after  $\sim 14.5$  ka.

239 T3 showed a very similar stratigraphy to T2 with poorly defined stratigraphic boundaries.  
240 Below a  $\sim 40$  cm soil cap, there was a further  $\sim 40$  cm of very uniform red clay without clasts.  
241 Beneath 80 cm depth, there were sparse fine gravels ( $< 3$  cm) in a clay matrix, with occasional  
242 cobbles up to  $\sim 20$  cm. Sample C6 (pit A3), a soil clast embedded in the uniform clay at  
243 a depth of  $\sim 76$  cm, yielded a calibrated age of 28.2–28.7 ka BP. Sample C7 (pit A3) at  
244 a depth of 88 cm yielded a calibrated age of 10.4–10.7 ka BP. These two samples are in  
245 reverse stratigraphic order, with a very large difference in age and one of similar age to C5  
246 on T2. This suggests that either C6 was eroded from up-slope and redeposited here during  
247 soil development or post-depositional contamination has occurred for one or both samples.

248 T4 has a 30 cm soil cap, and also merged slowly into a uniform red clay, which becomes  
249 interspersed with occasional small clasts below  $\sim 85$  cm. Two bulk samples, C8 of bulk soil

250 and C9 of bulk clay, yielded calibrated ages of 8.8–9.0 ka BP and 12.7–12.8 ka BP respectively  
251 – similar to samples from T2 and T3.

#### 252 2.1.4 Rc1 Terraces - Summary

253 Topographic profiles through the DEM of the Rc1 river valley with the present river gradient  
254 removed, reveal that T1, T2, T3 and T4 are offset vertically by  $\sim 10$ ,  $\sim 22$ ,  $\sim 45$  and  $\sim 53$   
255 metres respectively, relative to the present day footwall surface (Figure 4). In T1 and T2  
256 we note the back-tilting of the terrace surface in two locations, suggesting a progressive  
257 steepening of the fault plane in the uppermost 500 m of sediments, though we cannot  
258 constrain the absolute dips. Mild folding of the terrace surface in the 100–200 m south  
259 of the fault trace suggests a steep dip in the near surface, while the sinuous fault trace along  
260 the rangefront suggests that although the uppermost  $\sim 100$  m may be relatively steep, the  
261 section beneath most of the terraces should have a relatively low dip.

262 Radiocarbon samples constrain the age of the T1 surface to 4.1–9.7 ka, though as sug-  
263 gested by Thompson et al. (2002), we take the lower end of this as forming a close post-date  
264 on terrace formation, at  $\sim 4.1$  ka. This is similar to a prominent terrace dated at 4.2–5.2 ka  
265 in central Kyrgyzstan by Campbell (2015). Radiocarbon samples from the higher terraces  
266 proved more contextually difficult to interpret, but a sample from the gravel–clay inter-  
267 face on T2 gave an age of  $\sim 14$  ka. This would be consistent with T2 being the widespread  
268 QIII(3) terrace observed in Kyrgyzstan which is dated at 13.5–15.7 ka (Thompson et al.  
269 2002; Landgraf et al. 2016).

270 With the exception of C6 which is out of apparent stratigraphic order, the ages from T3  
271 and T4 are not significantly older than those observed for T2, suggesting that there was a  
272 major period of soil development at  $\sim 9$ –12 ka, responsible for all of these soil deposits; con-  
273 sistent with formation in the stable post-glacial conditions. Alternatively, extensive ground-  
274 water flow can result in post-depositional exchange of the carbon content, especially in  
275 bulk soil samples. The age inversion of C6 further suggests that reworking of material may

276 have occurred. Estimates of uplift and shortening rates based on the terrace sequence (and  
 277 predominantly on the lower terraces T1 and T2) are discussed in §2.4.

## 278 **2.2 River Catchment 2 – Border Valley (Rc2)**

279 The Pléiades DEM allowed us to extend our survey over a much larger area than was readily  
 280 achievable by field survey. The catchment Rc2 lies on the border between Kazakhstan and  
 281 Kyrgyzstan, and is therefore difficult to investigate thoroughly with a field survey. However,  
 282 the DEM reveals the exceptional level of preservation at this site, with 7 separate terrace  
 283 levels identified (Figure 6), sequentially uplifted by up to  $\sim 300$  m above present river level  
 284 (Figure 7). The degree of preservation is likely due to the river having the largest catchment  
 285 of any along the range front ( $\sim 1000$  km<sup>2</sup>). We label the terraces consistent with those at Rc1  
 286 and Rc3, based on uplift and morphology, but this correspondence is only approximate.

287 There is a large scarp at a primary fault strand at the range front, but the T2 surface also  
 288 shows a series of smaller offsets in the hanging wall, suggesting that a fraction of the motion  
 289 is distributed across the terrace surface. Each of the terraces also show a broad warping in  
 290 the immediate hanging wall over a wavelength of  $\sim 1.5$  km, suggesting either that the fault  
 291 dip flattens slightly towards the surface in the uppermost 1–2 km (Figure 6, 7), or that mild  
 292 folding of the hanging wall occurs.

293 The lowest terrace surface T0, records a vertical offset of just  $4.8 \pm 0.6$  m (Figure 7c),  
 294 the smallest observed along the range front. This young terrace is only well preserved within  
 295  $\sim 500$  m of the fault, so we are unable to assess any contributions due to folding. Addi-  
 296 tionally, we see a remnant of an intermediate terrace further upstream, displaying an offset  
 297 approximately half that of T2, which may be the T1 surface. This surface is displaced to  
 298  $16.7 \pm 2.5$  m above the present river level. Given the warping of the terrace surfaces, T0  
 299 could instead be the T1 surface, but with the surface slip reduced by slip on the secondary  
 300 structures.

301 The T2 terrace at Rc2 is very well preserved, extending  $\sim 2.5$  km upstream, with very  
 302 little incision/degradation. Given the similar level of preservation and degree of uplift, we

303 liken this terrace to the T2 terrace at Rc1. At the fault trace, we estimate a vertical offset of  
 304  $\sim 20$  m, but given the general folding of the terrace over the 2 km wavelength, we estimate  
 305 a maximum uplift of  $26 \pm 1.8$  m for T2.

306 The upper terraces T3–9 show similar shapes, though with a general progression towards  
 307 the basin of the point of maximum uplift of the terrace; we attribute this progression to  
 308 the advection of topography by fault motion. We estimate peak displacements of  $75 \pm 7$  m,  
 309  $102 \pm 4$  m,  $190 \pm 11$  m,  $304 \pm 22$  m for terraces T5, T6, T8 and T9 respectively.

### 310 **2.3 Results: River Catchment 3, Kyrgyzstan**

311 Catchment Rc3 is at the western end of the Karkara fault segment, in Kyrgyz territory  
 312 where the fault surface trace is  $\sim 15$  km from the Cenozoic/Palaeozoic contact (Figure 2).  
 313 The Rc3 river has a large catchment ( $\sim 360$  km<sup>2</sup>) and low gradient ( $0.9^\circ$ ), giving rise to large  
 314 fan structures and hence terrace surfaces.

#### 315 *2.3.1 Rc3: Terrace Offsets*

316 Figure 8 shows a detailed map of the major terrace surfaces observed at Rc3. The most  
 317 prominent terrace shows a similar morphology to the T2 terrace at Rc1 and Rc2 and a  
 318 similar scarp height, so we label this terrace T2 consistent with the previous sections. We  
 319 also identify a smaller terrace remnant  $\sim 700$  m from the fault trace which is approximately  
 320 half as high above the present river level as T2. We interpret this remnant as T1. The paired  
 321 T2 terrace is well preserved, extending  $\sim 10$  km upstream from the main fault trace (though  
 322 only  $\sim 4$  km is captured within the DEM, Figure 8a). A profile across the primary scarp on  
 323 the west side of the river (Figure 8c), shows an offset of  $13.0 \pm 0.4$  m relative to the modern  
 324 footwall. In addition to the main fault strand, we also observe a smaller scarp  $\sim 400$  m south  
 325 of the main scarp with an offset of  $2.4 \pm 0.4$  m (Figure 9d). Incorporating the secondary scarp  
 326 offset, we estimate a total vertical offset since abandonment of  $15.4 \pm 0.8$  m. On the eastern  
 327 side of the river channel, the fault trace splits in the older surfaces, forming a number of  
 328 smaller strands spread over  $\sim 1.5$  km.

329 On the eastern riverbank, a flight of four higher terraces is preserved, uplifted by up  
330 to 150 m above the current river channel. However, the fault is split into several strands  
331 (Figures 8,9), so each terrace surface shows scarps in several places. The high resolution  
332 Pléiades DEM enabled us to map terraces not visible in the field or satellite imagery. A  
333 perspective overview of the terrace system (Figure 9a) shows that these higher terraces are  
334 tilted eastwards, away from the main river channel, resulting in small channels which have  
335 formed at the base of the riser for each terrace. This might be due to curvature in the  
336 initial terrace surface at abandonment or differential uplift across the terrace system i.e. the  
337 terraces are folded but the fold axis plunges eastwards.

338 Scaling the peak displacement of T2 to match that of each of the higher terraces, we  
339 assign plausible labels to the higher terraces consistent with those at Rc2, T4–T8. However  
340 given the switching fault strands and the missing intermediate terraces there is considerable  
341 uncertainty in this labelling, so we are cautious of any interpretation relating the higher  
342 terraces to other sites. We estimate maximum offsets of 56 m, 78 m, 100 m, 120 m and  
343 150 m for the T4, T5, T6, T7 and T8 surfaces respectively (Figure 8d). We note that all  
344 the old terraces show similar displacement across the southern fault strand, while the older  
345 terraces show progressively more uplift on the northern strand than the younger ones. The  
346 youngest terraces T1 and T2 are continuous across the northern strand and are not offset  
347 across it. This suggests that fault motion used to be accommodated by the northern strand,  
348 but switched to the southern strand since the abandonment of T2.

### 349 *2.3.2 Rc3: Terrace Chronology*

350 The T2 terrace consists of a gravel bed deposited on a Neogene strath (exposed only in the  
351 river bed) capped with a thin ( $\sim 30$  cm) post-abandonment soil development. We sampled  
352 the surface via a pit near the primary fault trace, well away from any hillslopes above to  
353 minimise chance of redeposited material. The terrace gravels were broadly divided into two  
354 units; the upper with a soil matrix and the lower with a coarser sandy matrix, both with  
355 rounded clasts up to  $<35$  cm (Figure 9e,f). As at Rc1 (§2.1), we found two pockets of dark,

356 organic rich sediment embedded within the gravels. C1 at a depth of  $\sim 86$  cm yielded a  
357 calibrated age of 4.82–4.96 ka, while C2 at a depth of 105 cm yielded a calibrated age of  
358 26.99–27.45 ka. The large disparity in ages suggests post depositional mixing or significant  
359 groundwater leeching. Inspecting high resolution optical imagery available after the field  
360 investigation (Bing Maps), we note that there are remnant plough furrows on the majority  
361 of the terrace surface. This suggests the large, flat terrace surfaces were intensively farmed  
362 in the Soviet era so the upper part of the terrace may have undergone significant mixing in  
363 the last  $\sim 100$  years.

## 364 2.4 KRF Slip Rate

365 Figure 10 summarises the terrace ages we have constrained at Rc1 through radiocarbon  
366 dating, plotting terrace uplift against age. Based on the uplift of T1 and T2, we estimate an  
367 uplift rate of  $\sim 1.5$ – $2.6$  mm/yr (dashed lines, Figure 10). The ratios of the heights of T1 and  
368 T2 above the present river levels (§2.1) suggest that there was minimal burial in the footwall  
369 of the T2 surface, though the uplift of the T2 surface may still be underestimated by up to  
370 20% within the errors observed. The lower uplift rate suggested by T2 would suggest that  
371 some footwall burial may indeed have occurred. Also shown are the ages from the upper  
372 terraces T3 and T4 at Rc1 (grey points), which are mostly anomalously young and suggest  
373 a period of enhanced soil formation after the abandonment of T2. However, C6 would be  
374 consistent with a similar uplift rate to those suggested from T1 and T2, suggesting that it  
375 may have been unaffected by post-depositional carbon exchange.

376 Estimating a slip-rate and shortening rate for the fault remains difficult as we were  
377 unable to find fault exposure to estimate the fault dip. The relatively sinuous fault trace at  
378 a local scale suggests a gentle dip in the uppermost 100 m of sediment, though this is likely  
379 to steepen with depth, both as a ramp within the Cenozoic sediment sequence, and also  
380 as high-angle faulting within the basement rocks (c.f. basement faults are often found to  
381 be  $>45^\circ$  at depth, Avouac & Tapponnier 1993). Using Monte-Carlo simulations (Thompson  
382 et al. 2002), we estimate probability distribution functions (PDFs) for the slip-rate and

shortening rate based on conservative estimates for the fault dip, assuming that slip along the fault plane remains constant. In the shallow subsurface we take a dip range of 25–45° (uniform PDF). The fault most likely steepens within the basement so we assume a dip of 45–60° at depth.

We assume that T1 is well dated by sample C3, while T2 is bracketed with a uniform probability density function by the ages of C4 and C5, yielding a slip-rate of  $3.5_{-0.4}^{+1.7}$  mm/yr (or  $2.8_{-0.7}^{+1.4}$  mm/yr based on T2, Figure 10). We therefore estimate the shortening accommodated by the basement fault based to be  $2.3_{-0.6}^{+1.0}$  mm/yr from T1 ( $1.6_{-0.5}^{+1.1}$  mm/yr based on T2, 95% confidence bounds based on estimated PDFs, Figure 10).

### 3 KEGEN BASIN FOLD (KBF)

Approximately 12 km north from the main range front, a fold structure runs NE-SW through the middle of the Kegen Basin (KBF, Figures 1, 2, 11, 12), with a relief of 200–300 m above the basin floor. It may represent a foreland propagation structure from the main range front in a style similar to many basin folds observed in nearby Kyrgyzstan and China (e.g. Thompson et al. 2002; Charreau et al. 2008; Goode et al. 2011). The degree of bed rotation (described below) suggests that significant total slip has occurred, but the lack of Palaeozoic outcrop suggests that the fault is restricted to the basin sediments. Evaporitic layers are present in the deepest parts of the Cenozoic structure (identifiable in the satellite imagery as highly reflective in all bands), which may act as a decollement at depth (e.g. Bullen & Burbank 2001). We investigate the KBF, identifying Quaternary scarps along the northern edge and broad warping of a river terrace which crosses a large portion of it.

#### 3.1 KBF Structure and Geomorphology

Near the town of Karkara the KBF is cut by the Karkara river (large 1500 km<sup>2</sup> catchment), which has eroded a deep channel through the fold. River cut exposures into well bedded, steeply dipping Cenozoic deposits are preserved widely along the eastern riverbank and in several locations on the west (Figures 12a,b, 13a). We measured bedding orientations of

409 the Cenozoic sediments, in a profile nearly perpendicular to the fold, spanning the first  
 410 3.5 km south of the surface fault trace. The beds dip moderately to the north near the fault  
 411 ( $\sim 45^\circ$ ), steepening southwards to approximately vertical at  $\sim 3.4$  km S of the fault trace,  
 412 before switching to dip to the south (Figure 12c). Further south, the Cenozoic beds are no  
 413 longer well exposed because the river is less constrained by the channel through the fold  
 414 core, splitting into a number of smaller tributaries each with less incision such that there  
 415 are no natural exposures. Comparing the observed bedding dips to the topographic section  
 416 (Figure 12), we estimate a folding wavelength of  $\sim 6.5$  km, though much of the backlimb of  
 417 the fold has been eroded.

418 A prominent terrace on the eastern river bank (Figure 13a), is well preserved in both  
 419 the footwall and approximately 2 km into the hangingwall. Unfortunately only one short  
 420 terrace remnant was observed to the south of the fold axis, which we are unable to correlate  
 421 to other terraces so we can only estimate the deformation in the fore-limb of the fold. The  
 422 terraces consist of a strath cut into the Cenozoic beds overlain unconformably by river  
 423 gravels (Figure 13). Post terrace-abandonment, a loess cap (typically 0.5–2 m) accumulated,  
 424 followed by a soil development (0.1–0.5 m). We use kinematic GPS to measure a long profile  
 425 of the terrace surface (Figure 12c, location in Figure 11b). This was performed by car  
 426 along the road on the terrace surface, so the road embankment has resulted in an artificial  
 427 smoothing of the surface scarp. The terrace surface does not capture the crest of the folding  
 428 deformation, but we observe that folding has generated at least  $\sim 16$  m of uplift. Figure 13f  
 429 also shows a higher resolution pair of profiles across the fault scarp at the surface trace, from  
 430 which we estimate a vertical offset of  $10.0 \pm 0.5$  m, giving a minimum total uplift of  $\gtrsim 26$  m  
 431 since terrace abandonment.

### 432 3.2 KBF Chronology

433 Radiocarbon and OSL/IRSL samples were collected from the prominent river terrace cross-  
 434 ing the KBF (sampling locations in Figure 11). The individual luminescence and radiocarbon  
 435 ages are summarised in Tables 1–3.

*3.2.1 Radiocarbon Ages*

Samples C10 and C11 (sites A1, A2, Figure 11) consisted of amalgamated small fragments of gastropod shell from a sand lens within the gravels (Figure 13e), and yielded calibrated ages of 35.7–36.5 ka BP and 38.2–39.1 ka BP respectively. Gastropod shell has been shown to sometimes have significant inheritance due to the incorporation of calcium carbonate from the surrounding environment, or failure to behave as a closed system after burial (e.g. Pigati et al. 2010). In the nearby Saty valley, several modern (live) shells were dated at equivalent radiocarbon ages of 0–1000 yrs BP (Abdrakhmatov et al. 2016). Additionally, in dating amalgamated fragments, there is no well defined heritage, so there may be further inheritance due to post-death redeposition – dating of amalgamated small shell fragments by Abdrakhmatov et al. (2016) yielded ages of 4.5 ka and 8 ka for samples embedded in a medieval soil. As both C10 and C11 are within the terrace gravels and likely have significant inheritance, they only pose an upper limit on the abandonment age of the terrace.

*3.2.2 Luminescence Ages*

Sample OSL3 was collected from the base of the loess layer in a small channel of mixed loess/silt, cut into the terrace gravels (Figure 13c). OSL4 was collected from a coarse sand lens in the uppermost terrace gravels, deposited prior to terrace abandonment (Figure 13d). Both samples exhibited reasonably bright quartz OSL signals and dose recovery tests showed that in most cases a known dose could be recovered within 10% of the administered value without a systematic or strong trend with preheat temperature (see supplementary information S1). Though OSL4 was able to broadly recover a consistent dose, it showed significantly more scatter than OSL3. Of the 37 aliquots measured for OSL3, 17 were rejected on the basis of poor recycling ratios and a further 2 for excessive recuperation; the remaining 18 were used to calculate the equivalent dose. The poor recycling and recuperation were most likely due to the dominance of medium and slow components in those aliquots (see Supplement S1). OSL4 seemingly performed better, with only 1 of 25 aliquots rejected. We estimate quartz ages of  $15.2 \pm 1.1$  ka BP for OSL3, and  $22.6 \pm 1.4$  ka BP for OSL4 (Table 2).

463 In light of the mixed performance of the quartz OSL samples for samples from Rc1, IRSL  
464 and post-IR IRSL (pIRIR) measurements were carried out on K-feldspar extracts from the  
465 same samples (see methods in Supplement S1). The post-IR IRSL, with 225 degree second  
466 stimulation (pIRIR<sub>225</sub>) approach yielded ages of  $16.6\pm 0.9$  ka for OSL3 and  $33.0\pm 2.1$  for  
467 OSL4.

### 468 3.3 KBF Summary

469 The K-feldspar pIRIR<sub>225</sub>, fading corrected IRSL and quartz OSL agree closely for sample  
470 OSL3 within error, giving a post-date on the terrace abandonment of 14.1-17.5 ka BP.  
471 Samples C10, C11, and OSL4 are all expected to predate the terrace abandonment and  
472 range from 22–39 ka. However, given the poorer dose recovery rates for the quartz OSL of  
473 OSL4 and the significant departure from the feldspar pIRIR<sub>225</sub> results, the quartz age may  
474 be anomalously young. Our tightest pre-dating estimate is therefore the feldspar pIRIR<sub>225</sub>  
475 age of  $33.0\pm 2.1$  ka BP, consistent with samples C10 and C11 having significant inheritance  
476 of  $\sim 3.1$  and  $\sim 5.6$  ka respectively. Thus our age estimate for the terrace abandonment is  
477 14.1–35 ka, suggesting a minimum uplift rate of  $> 0.8$  mm/yr. However, as discussed by  
478 (Thompson et al. 2002) the date from the base of the post-abandonment deposits commonly  
479 gives the closest estimate to the terrace age so we might expect an age of  $\sim 15$ –17 ka, similar  
480 to the age of QIII(3), yielding an uplift rate of  $> 1.8$  mm/yr.

481 Unfortunately, there is no exposure of the fault driving the KBF and we only have  
482 structural observations in the core and forelimb of the fold so estimating a slip rate is  
483 difficult. The minimum uplift does suggest however a conservative minimum slip-rate of  
484 0.8 mm/yr (or 1.8 mm/yr if QIII(3)). This is still a moderately fast rate for the Tien Shan,  
485 so it is likely that this fold also accommodates a significant portion of the regional shortening  
486 in the uppermost crust.

487 **4 GPS CONSTRAINTS ON FAULT CREEP**

To estimate a present day geodetic slip-rate on the Karkara range front and investigate the possibility of fault creep, we fit an edge dislocation model to two N-S profiles through the regional GPS velocity field (Zubovich et al. 2010). The solution for the horizontal displacements ( $u_x$ ) at the surface due to a dipping semi-infinite edge dislocation at depth  $d$  in a uniform elastic halfspace (e.g. Segall 2010), is described by:

$$u_x = \frac{s}{\pi} \left( \cos \delta \arctan \eta + \frac{\sin \delta - \eta \cos \delta}{1 + \eta^2} \right) \quad , \quad (1)$$

$$\eta = \frac{x - d \cot \delta}{d} \quad , \quad (2)$$

488 where  $s$  is the fault slip,  $d$  is the depth to the edge dislocation,  $\delta$  is the fault dip and  $x$  is  
 489 the surface coordinate relative to the fault surface projection. This solution predicts surface  
 490 displacements for a fault plane locked down to a depth  $d$  and stably sliding below. As the  
 491 problem is linear, the case of a partially locked fault (e.g. with a slower slip rate on the  
 492 upper section than the lower section) can be treated as two planes slipping at different rates  
 493 superimposed to add to the correct slip rates. Similarly, changes in fault geometry can be  
 494 modelled as multiple edge dislocations superimposed.

495 We investigate profiles P and Q (Figure 1b) through the regional GPS data of Zubovich  
 496 et al. (2010), chosen to coincide with the highest density of stations within a swath of  $\pm 10$  km.  
 497 Before fitting the data, we subtract a regional strain rate of  $0.6 \times 10^{-15} \text{ s}^{-1}$  observed for this  
 498 region by England & Molnar (2015) – this extra component strain must be accommodated  
 499 by the faults of this region but is smoothly distributed and so cannot be attributed to any  
 500 individual fault.

501 *4.0.1 Profile Q-Q'*

502 Profile Q shows little or no curvature on either side of the fault, suggesting minimal lock-  
 503 ing. We know from Rc1 (§2.1) that the geometry of the fault in the uppermost  $\sim 1$  km of

504 sediments is not entirely constant, so the exact surface projection of the fault plane at seis-  
 505 mogenic depths is unlikely to coincide with the surface fault trace. The extreme scenario for  
 506 determining the locking depth is that the fault projects to half way between the two GPS  
 507 stations either side of the fault, so we use that fault location in order to put an maximum  
 508 bound on the locking depth.

509 We first perform a linear inversion for the slip rate with a zero locking depth and an  
 510 assumed fault dip of  $45^\circ$ , to estimate an approximate slip rate. This is refined by a grid  
 511 search in locking-depth – slip-rate space across a reasonable range. Our model estimates a  
 512 shortening-rate of  $3.2 \pm 0.3$  mm/yr, with a maximum locking depth of  $\sim 1.5$  km. The up-  
 513 permost 1–2 km is primarily composed of Cenozoic sediments, which are less likely to be  
 514 able to store significant elastic strain than the underlying crystalline basement rocks (e.g.  
 515 Tse & Rice 1986; Marone 1998), so it is likely that creep extends all the way to the sur-  
 516 face. Figure 14a shows the regional GPS data projected onto the line Q–Q', with our best  
 517 fit model overlain in red. The point in grey was excluded from the inversion, as it implies  
 518 localised extension across the thrust, though the model prediction is still within the 95%  
 519 error bound; the resultant rms misfit is 0.28 mm/yr. The black line shows a model locked  
 520 to a depth of 5 km, demonstrating that even relatively shallow locking is a poor fit to the  
 521 data. As creep appears to reach the surface at the full rate, the model is insensitive to the  
 522 fault dip. Estimates of the slip-rate are dip dependent, but our minimum of  $\sim 3.2$  mm/yr  
 523 makes it one of the fastest known in the Tien Shan.

#### 524 4.0.2 Profile P–P'

525 Profile P shows a large step offset at the fault (location well constrained), but it also shows  
 526 a broader deflection towards the fault over a wavelength of  $\sim 10$  km either side. This could  
 527 arise from two potential sources; partial locking of the upper fault plane and changes in fault  
 528 geometry. We test both of these cases and compare to that of a planar fault creeping all the  
 529 way to the surface.

530 Figure 14b shows the regional GPS data projected onto the line P–P' with our three best

531 fit models overlaid. A simple planar fault creeping to the surface at the full slip rate yields  
 532 a shortening rate of  $2.7\pm 0.6$  mm/yr, but does not give a good fit to the near fault stations  
 533 (rms misfit 0.36 mm/yr). If we allow partial locking above a depth  $D$ , we can solve for the  
 534 degree of locking ( $\epsilon$ ) and  $D$ . This model predicts a shortening rate of  $2.9\pm 0.7$  mm/yr, with  
 535  $\epsilon=0.7\pm 0.2$ , a poorly resolved locking depth of  $6_{-2}^{+3}$  km, and an rms misfit of 0.36 mm/yr.  
 536 Lastly, we superimpose a hypothetical model of changing geometry, with a constant slip  
 537 rate creeping to the surface. The data are not sufficient to constrain an inversion for the  
 538 geometries of such a model, but taking an example of a  $45^\circ$  fault at depth, which steepens  
 539 to  $60^\circ$  in the uppermost 7 km gives an rms error of 0.34 mm/yr, slightly lower than either  
 540 discussed above (Figure 14f).

541 We conclude that a single creeping fault does not provide a good fit to the available data  
 542 here and underestimates the slip rate, whereas a partially locked fault (slipping at 70% of  
 543 the full slip rate) or a flat-ramp geometry provide a better fit, with a shortening rate of  
 544  $2.9\pm 0.7$  mm/yr. Given the very close proximity of the stations either side of the fault on  
 545 this profile, a significant fraction of the fault slip is unambiguously reaching the surface at  
 546 the mapped fault strand. It is clear from both of the profiles discussed here that the KRF is  
 547 creeping, most likely at the full slip-rate resolvable from GPS at the present day (discussed  
 548 further in §5.1).

#### 549 4.1 GPS vs Late Quaternary Rate

550 Elastic halfspace modelling of the regional GPS velocity along profiles P and Q gives a  
 551 consistent shortening rate estimate of 2.9–3.2 mm/yr for both profiles. A careful inspection  
 552 of the regional GPS station locations shows that for profile Q (Figure 1), the only station  
 553 between the KBF surface trace and the KRF is a single one near the core of the fold that will  
 554 record little of the shortening accommodated by the KBF. Both profiles therefore include  
 555 any motion accommodated by both the KRF and the KBF and cannot distinguish between  
 556 them.

557 In §2.4 we estimated that the KRF has accommodated 1.1–3.3 mm/yr of shortening in the

late Quaternary. Without further estimates of the folding geometry at the KBF, we cannot convert our uplift estimate into a corresponding shortening rate – however, given its clear expression in the geomorphology, it is likely that it contributes a non-negligible component of shortening. Given the significant error margins in geochronology and fault geometry, our estimates of the shortening in the Late Quaternary are consistent with the geodetic rate. This suggests that the loading rate on these two faults has remained unchanged through time and, as they appear to together accommodate the 2.9–3.2 mm/yr of shortening seen in the GPS, it also suggests that they are creeping at their average long-term rate.

## 5 DISCUSSION

### 5.1 Creep on a Mature Fault

Modelling of the regional GPS data (§4) suggest that the KRF is either creeping or locked to shallow depths of <3-5 km. However, the time period of GPS observation is very short compared to the seismic cycle in the region (typically 1–5 ka, e.g. Abdрахmatov et al. 2001; Grützner et al. 2017a) so it is unclear whether the present creep is indicative of the long term fault behaviour.

In addition to the GPS data, the shape of the Late Quaternary fault scarp also hints at formation by creep over a longer timescale. The shape of the scarp in T1 at catchment Rc1 does not conform to a typical scarp diffusion model (e.g. Wallace 1977; Avouac 1993). The upper limb of the scarp shows a broadly curved shape as might be expected, but the lower limb shows very little curvature where it meets the footwall and the face of the scarp is very steep ( $\sim 21^\circ$ , Figure 4). This scarp shape instead fits the profile of a fresh scarp, with mild folding of the hangingwall and a gravity-controlled face at the base (e.g. Carretier et al. 2002). As the scarp would be large for a single event and there are no known events over the past hundred years on this fault, the scarp shape is consistent with continuous formation by fault creep, maintaining the ‘fresh’ appearance and gravity controlled face.

Most observations of creeping faults are from the decades to centuries following major earthquakes upon them (e.g. Cohn et al. 1982; Reilinger et al. 2000; Lienkaemper et al. 2001).

585 A number of major plate margin faults are also known deform by creep without associated  
586 earthquakes, for example sections of the North Anatolian fault (e.g. Kaneko et al. 2012),  
587 the Longitudinal Valley Fault (e.g. Thomas et al. 2014) and the San Andreas Fault (e.g.  
588 Steinbrugge et al. 1960; Titus et al. 2006). However, very few intraplate faults are observed to  
589 creep without a known prior earthquake (e.g. Jolivet et al. 2012; Copley & Jolivet 2016). The  
590 only known large historical earthquake close to the study area is the 1889 Chilik earthquake  
591 attributed to the Saty fault (e.g. Abdrakhmatov et al. 2016), see Figure 1 for its epicentre.  
592 There are no other known earthquakes which have occurred in the region of the Karkara  
593 Range front in the last few hundred years, but historic records in the region are generally  
594 short and poorly documented (Campbell et al. 2015).

595 The Main Terskey Front (MTF) is almost 600 km long, and at the longitude of the  
596 KRF it has considerable relief across the it. Apatite fission track (AFT) and apatite U–Th–  
597 Sm/He (AHe) ages suggest that the widespread late Cenozoic deformation initiated in the  
598 Tien Shan at  $\sim 25$  Ma (e.g. Hendrix et al. 1992; Yin et al. 1998), though recent studies in  
599 the vicinity of some of the major inherited structures suggest that tectonic deformation may  
600 have begun to occur as early as  $\sim 45$ – $55$  Ma (Glorie et al. 2011). Macaulay et al. (2014)  
601 suggest that deformation initiated on the inherited structures best able to accommodate  
602 the regional deformation, including the MTF on the northern front of the Terskey Range.  
603 Samples from the Terskey Range show an intensification in the late Cenozoic, driven by  
604 increased regional shortening (5–3 Ma, Sobel et al. 2006; Selander et al. 2012; Macaulay  
605 et al. 2014). The AFT data show rapid bedrock exhumation in the Terskey Range over the  
606 late Cenozoic, our results show a rapid slip-rate on the KRF through the late Quaternary,  
607 and the regional GPS suggest rapid slip at the present. The MTF therefore appears to have  
608 played and be playing a major role in the development of the Tien Shan – a very mature  
609 fault that has accommodated significant total displacement. This is consistent with the other  
610 major examples of long term creep on intraplate faults (e.g. San Andreas, North Anatolian  
611 Fault), suggesting that the fault maturity is linked to its strength (Bürgmann & Dresen

2008), allowing deformation by aseismic creep (e.g. Chester et al. 1993; Kaneko et al. 2012; Carpenter et al. 2011).

## 5.2 Seismic Hazard

The observed shortening rate makes the Karkara Rangefront one of the fastest faults in the Tien Shan, though even faster rates are observed further SW in the Pamir (Arrowsmith & Strecker 1999). Our observations show that most or all of the slip is reaching the surface as creep, suggesting that strain accumulation across the fault is likely to be minimal at present. Seismic hazard assessments based on the regional strain rate field (e.g. Holt et al. 2005) may overestimate the seismic hazard in the area, as a significant fraction of the strain is being released aseismically and creep manifests as an extremely high strain rate. However, the capacity for creeping faults to sustain large earthquakes is debated (e.g. Harris 2017; Chen & Bürgmann 2017) and as noted above, it is not clear whether creep is the long term deformation mechanism.

Contemporary studies of the late-Quaternary faulting in the Tien Shan have mostly focused on the western and northern ranges of Kyrgyzstan (e.g. Burtman et al. 1996; Burbank et al. 1999; Abdrakhmatov et al. 2002; Thompson et al. 2002; Oskin & Burbank 2007; Selander et al. 2012; Goode et al. 2014; Landgraf et al. 2016) and the Chinese Tien Shan (e.g. Burchfiel et al. 1999; Hubert-Ferrari 2005). Fewer studies have focused on the Tien Shan of SE Kazakhstan (e.g. Arrowsmith et al. 2016; Abdrakhmatov et al. 2016; Grützner et al. 2017b) and there are few known slip rates on the active faults in the region (Campbell et al. 2013; Cording et al. 2014). It is likely that many more faults are unmapped or unrecognised as active (Grützner et al. 2017a).

While it appears from the GPS data that the KRF is creeping at the full slip-rate at present, the resolution of GPS is limited and as previously noted there is a regional velocity gradient that must also be accommodated by the faults of the region but cannot be attributed to any individual fault. By comparison, none of the other faults across the Tien Shan are well resolved in the GPS velocity field and yet they have accommodated several large (M8+)

639 earthquakes in the past few hundred years (Figure 1, e.g. Delvaux et al. 2001; Campbell et al.  
640 2015; Abdrakhmatov et al. 2016). Thus, there may still be a degree of strain accumulation  
641 below the resolution limit of GPS, which could result in earthquakes. In addition, faults such  
642 as the Longitudinal Valley Fault have been shown to sustain earthquakes which nucleate in  
643 non-creeping velocity-weakening regions but propagate into velocity strengthening regions  
644 that deform primarily by creep (e.g. Thomas et al. 2014).

645 The greater rangefront of the Terskey Range is almost 600 km in length. It is unclear  
646 how far along this structure ruptures could propagate, though the section we primarily  
647 focus on in this study is  $\sim 40$  km without significant stepovers, suggesting a lower bound. If  
648 multiple segments can rupture together, however, we could expect large magnitude events.  
649 The evidence suggests that creep is accommodating a large fraction of the fault slip rate  
650 at present, which may be the long term mechanism for slip on this fault, but palaeoseismic  
651 excavation is required to ascertain whether the fault can sustain earthquakes. The majority  
652 of the primary scarps observed along the Karkara rangefront are very large to be attributable  
653 to single earthquake events – most terraces are uplifted by  $>10$  m. The only exceptions are  
654 the river knick point at Rc1 with a relatively diffuse deflection of  $2.5 \pm 0.5$  m (§2.1) and a  
655 terrace offset by  $4.8 \pm 0.6$  m at Rc3 (§2.2). In most catchments (Rc1–3) we map multiple small  
656 secondary scarps south of the main fault trace with offsets of 1-2 m; these are consistent with  
657 hangingwall accommodation structures but it is unclear whether they are formed seismically.

658 At Rc3, the small scarp of  $\sim 5$  m and the numerous secondary scarps warrant further  
659 field investigation. The secondary scarps in particular present targets for palaeoseismology,  
660 as they may allow development of an earthquake record on a rangefront where the primary  
661 scarps are generally too large for trenching.

662 It is important to note that the GPS velocities of Zubovich et al. (2010) give excep-  
663 tionally dense coverage and the duration of the campaigns has resulted in small errors –  
664 there are few surveys of equivalent quality elsewhere. It is therefore quite possible that other  
665 intracontinental faults such as the KRF are creeping, but we are unable to resolve them  
666 with present geodetic data. Further work is needed along the KRF to further characterise

667 the spatial extent and temporal evolution of the observed fault creep – it offers a unique  
668 opportunity to probe the frictional behaviour of a mature fault in an intracontinental setting.

## 669 6 CONCLUSIONS

670 We estimate a Late Quaternary slip rate on the Karkara Rangefront Fault of  $3.5_{-0.4}^{+1.7}$  mm/yr  
671 and a minimum uplift rate of 0.8 mm/yr (though possibly as large as 1.8 mm/yr) at the  
672 core of the Kegen Basin Fold. Based on a conservative estimate of a steeply dipping base-  
673 ment fault, we estimate a minimum equivalent shortening rate of 1.1–3.3 mm/yr across the  
674 rangefront. This is the fastest known fault slip-rate in the northern Tien Shan, but elastic  
675 halfspace modelling of the regional GPS shows that at present this is mostly accommodated  
676 by creep, suggesting that there is minimal strain accumulation at present within GPS reso-  
677 lution. We attribute the velocity strengthening properties of the fault necessary for creep to  
678 the mature nature of the Main Terskey Front.

679 Major earthquakes (M8+) have occurred in the past two centuries on other faults in the  
680 region that are completely unresolved in the regional GPS velocity field, so this fault may  
681 still be capable of earthquakes – further palaeoseismic investigation is necessary. This study  
682 also highlights the need for dense regional GPS surveys to identify creep – there may be  
683 many creeping faults unidentified due to the sparsity of GPS networks in intra-plate regions.

## 684 ACKNOWLEDGMENTS

685 This work was supported by funding from the UK Natural Environment Research Council  
686 (NERC) through the Looking Inside the Continents (LiCS) project (NE/K011006/1), the  
687 Earthquake without Frontiers (EwF) project (EwF\_NE/J02001X/1.1), and the Centre for  
688 the Observation and Modelling of Earthquakes, Volcanoes and Tectonics (COMET) project  
689 (COME30001, <http://comet.nerc.ac.uk>). RTW also acknowledges support from the Royal  
690 Society. Many of the figures were made using the public domain software Generic Map-  
691 ping Tools (Wessel & Smith 1998). Analysis and visualisation of the DEMs and elevation  
692 pointclouds was performed using the KeckCaves virtual reality software suite.

693 **REFERENCES**

- 694 Abdrakhmatov, K., Weldon, R. J., Thompson, S. C., Burbank, D. W., Rubin, C., Miller, M., &  
695 Molnar, P., 2001. Onset, style and current rate of shortening in the central Tien Shan, Kyrgyz  
696 Republic, *Russian Geology and Geophysics*, **42**(10), 1585–1609.
- 697 Abdrakhmatov, K., Walker, R., Campbell, G., Carr, A., Elliott, A., Hillemann, C., Hollingsworth,  
698 J., Landgraf, A., Mackenzie, D., Mukambayev, A., Rizza, M., & Sloan, R., 2016. Multi-segment  
699 rupture in the July 11th 1889 Chilik earthquake (Mw 8.0-8.3), Kazakh Tien Shan, interpreted  
700 from remote-sensing, field survey, and palaeoseismic trenching, *Journal of Geophysical Research:*  
701 *Solid Earth*.
- 702 Abdrakhmatov, K. E., Djanuzakov, K. D., & Delvaux, D., 2002. Active Tectonics and Seismic  
703 Hazard of the Issyk-Kul Basin in the Kyrgyz Tian-Shan, in *Lake Issyk-Kul: Its Natural Envi-*  
704 *ronment*, pp. 147–160, Springer Netherlands, Dordrecht.
- 705 Abdrakhmatov, K. Y., Aldazhanov, S. A., Hager, B. H., Hamburger, M. W., Herring, T. A.,  
706 Kalabaev, K. B., Makarov, V. I., & Molnar, P., 1996. Relatively recent construction of the  
707 Tien Shan inferred from GPS measurements of present-day crustal deformation rates, *Letters to*  
708 *Nature*, **384**.
- 709 Arrowsmith, J. R. & Strecker, M. R., 1999. Seismotectonic range-front segmentation and  
710 mountain-belt growth in the Pamir-Alai region , Kyrgyzstan ( India-Eurasia collision zone ),  
711 *Geological Society of America*, **111**(11), 1665–1683.
- 712 Arrowsmith, J. R., Crosby, C. J., Korzhenkov, A. M., Mamurov, E., Povolotskaya, I., Guralnik,  
713 B., & Landgraf, A., 2016. Surface rupture of the 1911 Kebin (ChonKemin) earthquake, Northern  
714 Tien Shan, Kyrgyzstan, *Geological Society, London, Special Publications*.
- 715 Avouac, J.-P., 1993. Analysis of scarp profiles: Evaluation of errors in morphologic dating, *Journal*  
716 *of Geophysical Research*, **98**(B4), 6745.
- 717 Avouac, J.-P., 2015. From Geodetic Imaging of Seismic and Aseismic Fault Slip to Dynamic  
718 Modeling of the Seismic Cycle, *Annual Review of Earth and Planetary Sciences*, **43**(1), 233–  
719 271.
- 720 Avouac, J.-P. & Tapponnier, P., 1993. Kinematic model of active deformation in central Asia,  
721 *Geophysical Research Letters*, **20**(10), 895–898.
- 722 Bronk Ramsey, C., 2009. Bayesian Analysis of Radiocarbon Dates, *Radiocarbon*, **51**(1), 337–360.
- 723 Bullen, M. & Burbank, D., 2001. Late Cenozoic tectonic evolution of the northwestern Tien  
724 Shan: New age estimates for the initiation of mountain building, *Geological Society of America*  
725 *Bulletin*, **113**(12), 1544–1559.
- 726 Burbank, McLean, Bullen, Abdrakhmatov, & Miller, 1999. Partitioning of intermontane basins  
727 by thrust-related folding, Tien Shan, Kyrgyzstan, *Basin Research*, **11**(1), 75–92.

- 728 Burbank, D. W. & Anderson, R. S., 2011. *Tectonic Geomorphology*, John Wiley & Sons, Ltd,  
729 Chichester, UK.
- 730 Burchfiel, B. C., Brown, E. T., Qidong, D., Xianyue, F., Jun, L., Molnar, P., Jianbang, S., Zhang-  
731 ming, W., & Huichuan, Y., 1999. Crustal Shortening on the Margins of the Tien Shan, Xinjiang,  
732 China, *International Geology Review*, **41**(January), 665–700.
- 733 Bürgmann, R. & Dresen, G., 2008. Rheology of the Lower Crust and Upper Mantle: Evidence  
734 from Rock Mechanics, Geodesy, and Field Observations, *Annual Review of Earth and Planetary  
735 Sciences*, **36**(1), 531–567.
- 736 Burtman, V. S., Skobelev, S. F., & Molnar, P., 1996. Late Cenozoic slip on the Talas-Ferghana  
737 fault, the Tien Shan, central Asia, *Geological Society of America Bulletin*, **108**(8), 1004–1021.
- 738 Campbell, G., 2015. *Active Tectonics of the Tien Shan, Central Asia*, Ph.D. thesis, University of  
739 Cambridge.
- 740 Campbell, G. E., Walker, R. T., Abdrakhmatov, K., Schwenninger, J., Jackson, J., Elliott, J. R.,  
741 & Copley, A., 2013. The Dzhungarian fault: Late Quaternary tectonics and slip rate of a major  
742 right-lateral strike-slip fault in the northern Tien Shan region, *Journal of Geophysical Research:  
743 Solid Earth*, **118**, 5681–5698.
- 744 Campbell, G. E., Walker, R. T., Abdrakhmatov, K., Jackson, J., Elliott, J. R., Mackenzie, D.,  
745 Middleton, T., & Schwenninger, J.-L., 2015. Great earthquakes in low strain rate continental in-  
746 teriors: An example from SE Kazakhstan, *Journal of Geophysical Research: Solid Earth*, **120**(8),  
747 5507–5534.
- 748 Carpenter, B. M., Marone, C., & Saffer, D. M., 2011. Weakness of the San Andreas Fault revealed  
749 by samples from the active fault zone, *Nature Geoscience*, **4**(4), 251–254.
- 750 Carretier, S., Ritz, J. F., Jackson, J., & Bayasgalan, A., 2002. Morphological dating of cumula-  
751 tive reverse fault scarps: Examples from the Gurvan Bogd fault system, Mongolia, *Geophysical  
752 Journal International*, **148**(2), 256–277.
- 753 Charreau, J., Avouac, J. P., Chen, Y., Dominguez, S., & Gilder, S., 2008. Miocene to present  
754 kinematics of fault-bend folding across the Huerguosi anticline, northern Tianshan (China),  
755 derived from structural, seismic, and magnetostratigraphic data, *Geology*, **36**(11), 871–874.
- 756 Chen, K. H. & Bürgmann, R., 2017. Creeping faults: Good news, bad news?, *Reviews of Geo-  
757 physics*, **55**(2), 282–286.
- 758 Chester, F. M., Evans, J. P., & Biegel, R. L., 1993. Internal structure and weakening mechanisms  
759 of the San Andreas Fault, *Journal of Geophysical Research*, **98**(B1), 771.
- 760 Cohn, B. S. N., Allen, C. R., Oilman, R., & Goultly, N. R., 1982. Preearthquake and postearthquake  
761 creep on the imperial fault and the brawley fault zone, in *The Imperial Valley, California,  
762 earthquake of October 15, 1979. Geological Survey professional paper. No.1254*, pp. 161–167,

- 763 United States Geological Survey, Washington, DC.
- 764 Copley, A. & Jolivet, R., 2016. Fault rheology in an aseismic fold-thrust belt (Shahdad, eastern  
765 Iran), *Journal of Geophysical Research: Solid Earth*, **121**(1), 412–431.
- 766 Cording, A., Hetzel, R., Kober, M., & Kley, J., 2014. <sup>10</sup>Be exposure dating of river terraces at  
767 the southern mountain front of the Dzungarian Alatau (SE Kazakhstan) reveals rate of thrust  
768 faulting over the past ~400ka, *Quaternary Research*, **81**(1), 168–178.
- 769 Delvaux, D., Abdrakhmatov, K., Lemzin, I., & Strom, A., 2001. Landslides and surface breaks  
770 af the Ms 8.2 Kemin earthquake (Kyrgyzstan), *Russian Geology and Geophysics*, **42**(10), 1583–  
771 1592.
- 772 Deng, Q., Zhang, P., Ran, Y., Yang, X., Min, W., & Chu, Q., 2003. Basic characteristics of active  
773 tectonics of China, *Science in China (Series D)*, **46**(4), 356–372.
- 774 Deng, Q., Ran, Y., Yang, X., Min, W., & Chu, Q., 2004. Map of Active Tectonics in China (in  
775 Chinese).
- 776 England, P. & Molnar, P., 2015. Rheology of the lithosphere beneath the central and western  
777 Tien Shan, *Journal of Geophysical Research: Solid Earth*, **120**(5), 3803–3823.
- 778 Gebhardt, A. C., Naudts, L., Mol, L. D., Klerkx, J., Abdrakhmatov, K., Sobel, E. R., & De Batist,  
779 M., 2017. High-amplitude lake-level changes in tectonically active Lake Issyk-Kul ( Kyrgyzstan  
780 ) revealed by high-resolution seismic reflection data, *Climate of the Past*, **13**, 73–92.
- 781 Glorie, S., De Grave, J., Buslov, M. M., Zhimulev, F. I., Stockli, D. F., Batalev, V. Y., Izmer, A.,  
782 Van den haute, P., Vanhaecke, F., & Elburg, M. A., 2011. Tectonic history of the Kyrgyz South  
783 Tien Shan (Atbashi-Inylchek) suture zone: The role of inherited structures during deformation-  
784 propagation, *Tectonics*, **30**(6).
- 785 Goode, J. K., Burbank, D. W., & Bookhagen, B., 2011. Basin width control of faulting in the  
786 Naryn Basin, south-central Kyrgyzstan, *Tectonics*, **30**(6).
- 787 Goode, J. K., Burbank, D. W., & Ormukov, C., 2014. Pliocene-Pleistocene initiation, style, and  
788 sequencing of deformation in the central Tien Shan, *Tectonics*, **33**(4), 464–484.
- 789 Grützner, C., Carson, E., Walker, R., Rhodes, E., Mukambayev, A., Mackenzie, D., Elliott, J.,  
790 Campbell, G., & Abdrakhmatov, K., 2017a. Assessing the activity of faults in continental  
791 interiors: Palaeoseismic insights from SE Kazakhstan, *Earth and Planetary Science Letters*,  
792 **459**, 93–104.
- 793 Grützner, C., Walker, R. T., Abdrakhmatov, K. E., Mukambaev, A., Elliott, A. J., & Elliott, J. R.,  
794 2017b. Active tectonics around Almaty and along the Zailisky Alatau rangefront, *Tectonics (In*  
795 *Press)*.
- 796 Harris, R. A., 2017. Large earthquakes and creeping faults, *Reviews of Geophysics*, **55**(1), 169–198.
- 797 Hendrix, M. S., Graham, S. A., Carroll, A. R., Sobel, E. R., McKnight, C. L., Schulein, B. J.,

- 798 & Wang, Z., 1992. Sedimentary record and climatic implications of recurrent deformation in  
799 the Tian Shan: Evidence from Mesozoic strata of the north Tarim, south Junggar, and Turpan  
800 basins, northwest China, *Geological Society of America Bulletin*, **104**(1), 53–79.
- 801 Holt, W. E., Kreemer, C., Haines, a. J., Estey, L., Meertens, C., Blewitt, G., & Lavallée, D., 2005.  
802 Project helps constrain continental dynamics and seismic hazards, *Eos, Transactions American*  
803 *Geophysical Union*, **86**(41), 383.
- 804 Hubert-Ferrari, A., 2005. Irregular earthquake cycle along the southern Tianshan front, Aksu  
805 area, China, *Journal of Geophysical Research*, **110**(B6), B06402.
- 806 Jolivet, R., Lasserre, C., Doin, M. P., Guillaso, S., Peltzer, G., Dailu, R., Sun, J., Shen, Z. K., & Xu,  
807 X., 2012. Shallow creep on the Haiyuan fault (Gansu, China) revealed by SAR interferometry,  
808 *Journal of Geophysical Research: Solid Earth*, **117**(6), 1–18.
- 809 Kaneko, Y., Fialko, Y., Sandwell, D. T., Tong, X., & Furuya, M., 2012. Interseismic deformation  
810 and creep along the central section of the North Anatolian fault (Turkey): InSAR observations  
811 and implications for rate-and-state friction properties, *Journal of Geophysical Research*, **118**,  
812 1–15.
- 813 Landgraf, A., Dzhumabaeva, A., Abdrakhmatov, K. E., Strecker, M. R., Macaulay, E. A., Arrow-  
814 smith, J. R., Sudhaus, H., Preusser, F., Rugel, G., & Merchel, S., 2016. Repeated large-magnitude  
815 earthquakes in a tectonically active, low-strain continental interior: the northern Tien Shan, Kyr-  
816 gyzstan, *Journal of Geophysical Research: Solid Earth*, pp. 1–23.
- 817 Le Béon, M., Suppe, J., Jaiswal, M. K., Chen, Y.-G., & Ustaszewski, M. E., 2014. Deciphering  
818 cumulative fault slip vectors from fold scarps: Relationships between long-term and coseismic  
819 deformations in central Western Taiwan, *Journal of Geophysical Research: Solid Earth*, **119**(7),  
820 5943–5978.
- 821 Lienkaemper, J. J., Galehouse, J. S., & Simpson, R. W., 2001. Long-term monitoring of creep  
822 rate along the Hayward fault and evidence for a lasting creep response to 1989 Loma Prieta  
823 earthquake, *Geophysical Research Letters*, **28**(11), 2265–2268.
- 824 Macaulay, E. A., Sobel, E. R., Mikolaichuk, A., Landgraf, A., Kohn, B., & Stuart, F., 2013.  
825 Thermochronologic insight into late Cenozoic deformation in the basement-cored Terskey Range,  
826 Kyrgyz Tien Shan, *Tectonics*, **32**(3), 487–500.
- 827 Macaulay, E. A., Sobel, E. R., Mikolaichuk, A., Kohn, B., & Stuart, F. M., 2014. Cenozoic  
828 deformation and exhumation history of the Central Kyrgyz Tien Shan, *Tectonics*, **33**(2), 135–  
829 165.
- 830 Mackenzie, D., Abdrakhmatov, K., Campbell, G., Grützner, C., Carson, E., & Moldobaeb, A.,  
831 2015. A transect of quaternary geological slip rates in the Kazakh Tien Shan, in *6th International*  
832 *INQUA Meeting on Paleoseismology, Active Tectonics and Archaeoseismology*, no. April, pp.

833 267–270.

834 Marone, C., 1998. Laboratory-Derived Friction Laws and Their Application To Seismic Faulting,  
835 *Annual Review of Earth and Planetary Sciences*, **26**(1), 643–696.

836 Oskin, M. E. & Burbank, D., 2007. Transient landscape evolution of basement-cored uplifts:  
837 Example of the Kyrgyz Range, Tian Shan, *Journal of Geophysical Research*, **112**(F03S03).

838 Pigati, J. S., Rech, J. A., & Nekola, J. C., 2010. Radiocarbon dating of small terrestrial gastropod  
839 shells in North America, *Quaternary Geochronology*, **5**(5), 519–532.

840 Reid, H. F., 1910. The mechanics of the earthquake, The California Earthquake of April 18, 1906:  
841 *Report of the State Earthquake Investigation Commission*, **2**(87).

842 Reilinger, R. E., Ergintav, S., Burgmann, R., McClusky, S., Lenk, O., Barka, A., Gurkan, O.,  
843 Hearn, L., Feigl, K. L., Cakmak, R., Aktug, B., Ozener, H., & Toksoz, M. N., 2000. Coseismic  
844 and Postseismic Fault Slip for the 17 August 1999, M = 7.5, Izmit, Turkey Earthquake, *Science*,  
845 **289**(5484), 1519–1524.

846 Reimer, P., 2013. IntCal13 and Marine13 Radiocarbon Age Calibration Curves 0-50,000 Years  
847 cal BP, *Radiocarbon*, **55**(4), 1869–1887.

848 Segall, P., 2010. *Earthquake and volcano deformation*, Princeton University Press.

849 Selander, J., Oskin, M., Ormukov, C., & Abdrakhmatov, K., 2012. Inherited strike-slip faults  
850 as an origin for basement-cored uplifts: Example of the Kungey and Zailiskey ranges, northern  
851 Tian Shan, *Tectonics*, **31**(4).

852 Smith, S. W. & Wyss, M., 1968. Displacement on the San Andreas fault subsequent to the 1966  
853 Parkfield earthquake, *Bulletin of the Seismological Society of America*, **58**(6), 1955–1973.

854 Sobel, E. R., Oskin, M., Burbank, D., & Mikolaichuk, A., 2006. Exhumation of basement-cored  
855 uplifts: Example of the Kyrgyz Range quantified with apatite fission track thermochronolgy,  
856 *Tectonics*, **25**(2).

857 Steinbrugge, K. V., Zacher, E. G., Tocher, D., Whitten, C. A., & Claire, C. N., 1960. Creep on  
858 the San Andreas Fault, *Bulletin of the Seismological Society of America*, **50**(3), 389–396.

859 Takaku, J., Tadono, T., & Tsutsui, K., 2014. Generation of High Resolution Global DSM from  
860 ALOS PRISM, *ISPRS - International Archives of the Photogrammetry, Remote Sensing and*  
861 *Spatial Information Sciences*, **XL-4**(4), 243–248.

862 Tapponnier, P. & Molnar, P., 1979. Active faulting and cenozoic tectonics of the Tien Shan,  
863 Mongolia, and Baykal Regions, *Journal of Geophysical Research: Solid Earth*, **84**(B7), 3425–  
864 3459.

865 Thatcher, W., 1983. Nonlinear strain buildup and the earthquake cycle on the San Andreas Fault,  
866 *Journal of Geophysical Research: Solid Earth*, **88**(B7), 5893–5902.

867 Thomas, M. Y., Avouac, J.-P., Champenois, J., Lee, J.-C., & Kuo, L.-C., 2014. Spatiotemporal

- 868 evolution of seismic and aseismic slip on the Longitudinal Valley Fault, Taiwan, *Journal of*  
869 *Geophysical Research: Solid Earth*, **119**(6), 5114–5139.
- 870 Thompson, S. C., Weldon, R. J., Rubin, C. M., Abdrakhmatov, K., Molnar, P., & Berger, G. W.,  
871 2002. Late Quaternary slip rates across the central Tien Shan, Kyrgyzstan, central Asia, *Journal*  
872 *of Geophysical Research*, **107**(B9), 2203.
- 873 Titus, S. J., DeMets, C., & Tikoff, B., 2006. Thirty-five-year creep rates for the creeping seg-  
874 ment of the San Andreas fault and the effects of the 2004 Parkfield earthquake: Constraints  
875 from alignment arrays, continuous global positioning system, and creepmeters, *Bulletin of the*  
876 *Seismological Society of America*, **96**(4 B), 250–268.
- 877 Tse, S. T. & Rice, J. R., 1986. Crustal earthquake instability in relation to the depth variation  
878 of frictional slip properties, *Journal of Geophysical Research*, **91**(B9), 9452–9472.
- 879 Wallace, R. E., 1977. Profiles and ages of young fault scarps, north-central Nevada, *Geological*  
880 *Society of America Bulletin*, **88**(9), 1267.
- 881 Wessel, P. & Smith, W. H. F., 1998. New, improved version of generic mapping tools released,  
882 *Eos, Transactions American Geophysical Union*, **79**(47), 579–579.
- 883 Yin, A., Nie, S., Craig, P., Harrison, T. M., Ryerson, F. J., Xianglin, Q., & Geng, Y., 1998. Late  
884 Cenozoic tectonic evolution of the southern Chinese Tian Shan, *Tectonics*, **17**(1), 1–27.
- 885 Zubovich, A. V., Wang, X.-Q., Scherba, Y. G., Schelochkov, G. G., Reilinger, R., Reigber, C.,  
886 Mosienko, O. I., Molnar, P., Michajljow, W., Makarov, V. I., Li, J., Kuzikov, S. I., Herring,  
887 T. A., Hamburger, M. W., Hager, B. H., Dang, Y.-M., Bragin, V. D., & Beisenbaev, R. T., 2010.  
888 GPS velocity field for the Tien Shan and surrounding regions, *Tectonics*, **29**(6).

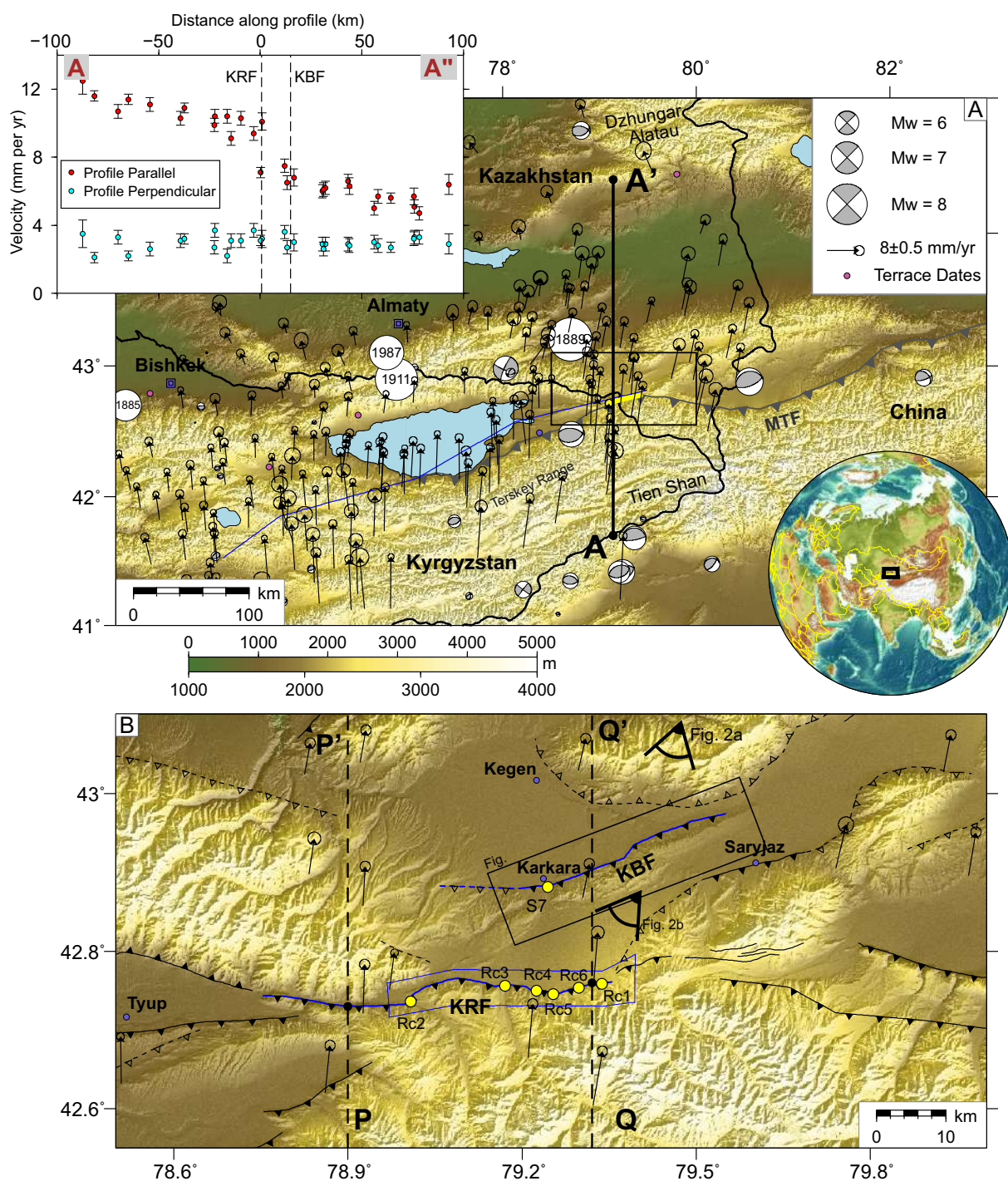


**Figure 1.** (top) An overview of the NE Tien Shan. Historic earthquakes of  $M > 6$  are shown as open circles, and focal mechanisms show modern instrumental earthquakes of  $M > 6$  from the global centroid moment tensor (GCMT) catalogue. GPS velocity vectors are from Zubovich et al. (2010) and ellipses indicate the 95% confidence interval. The blue line represents the discrete step in the northwards regional GPS velocities identified by England & Molnar (2015). (inset) GPS velocity vectors over a swath width of  $\pm 40$  km projected on to the line A–A'. Dashed line indicates the surface fault location. Error bars indicate the 95% confidence interval. Modified after Mackenzie et al. (2015). (bottom) Inset showing the Karkara Range (KRF), the Kegen Basin Fold (KBF), and the individual study sites Rc1–3. Blue outline shows the extents of the stereo Pléiades derived DEM. Profiles P–P' and Q–Q' are the two profiles taken through the regional GPS velocity field, modelled to estimate the fault creep rate (Figure 14).

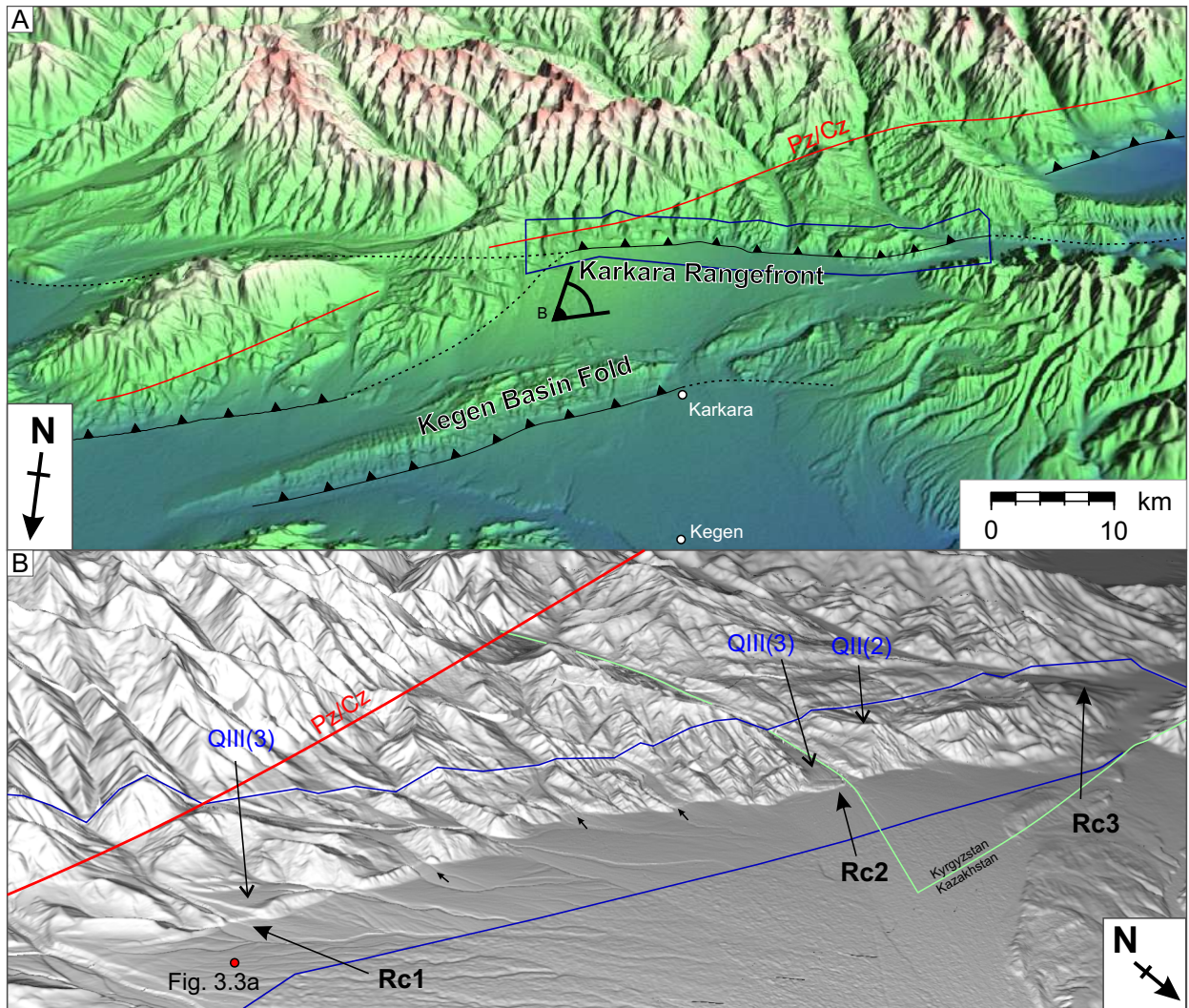


**Figure 2.** (a) Perspective view of the Terskey northern rangefront, showing the major structures studied here. Basemap elevation data from the SRTM 1-second dataset. 2x vertical exaggeration. Red line indicates the Palaeozoic–Cenozoic contact at the surface for the Karkara Rangefront. (b) Perspective view looking SW along the KRF, from the Pléiades derived DEM on top of the AW3D30 DEM (Takaku et al. 2014), showing the individual river catchments studied. Minor arrows indicate the catchments described in Supplement S2. Blue lines outline of the high resolution dataset.

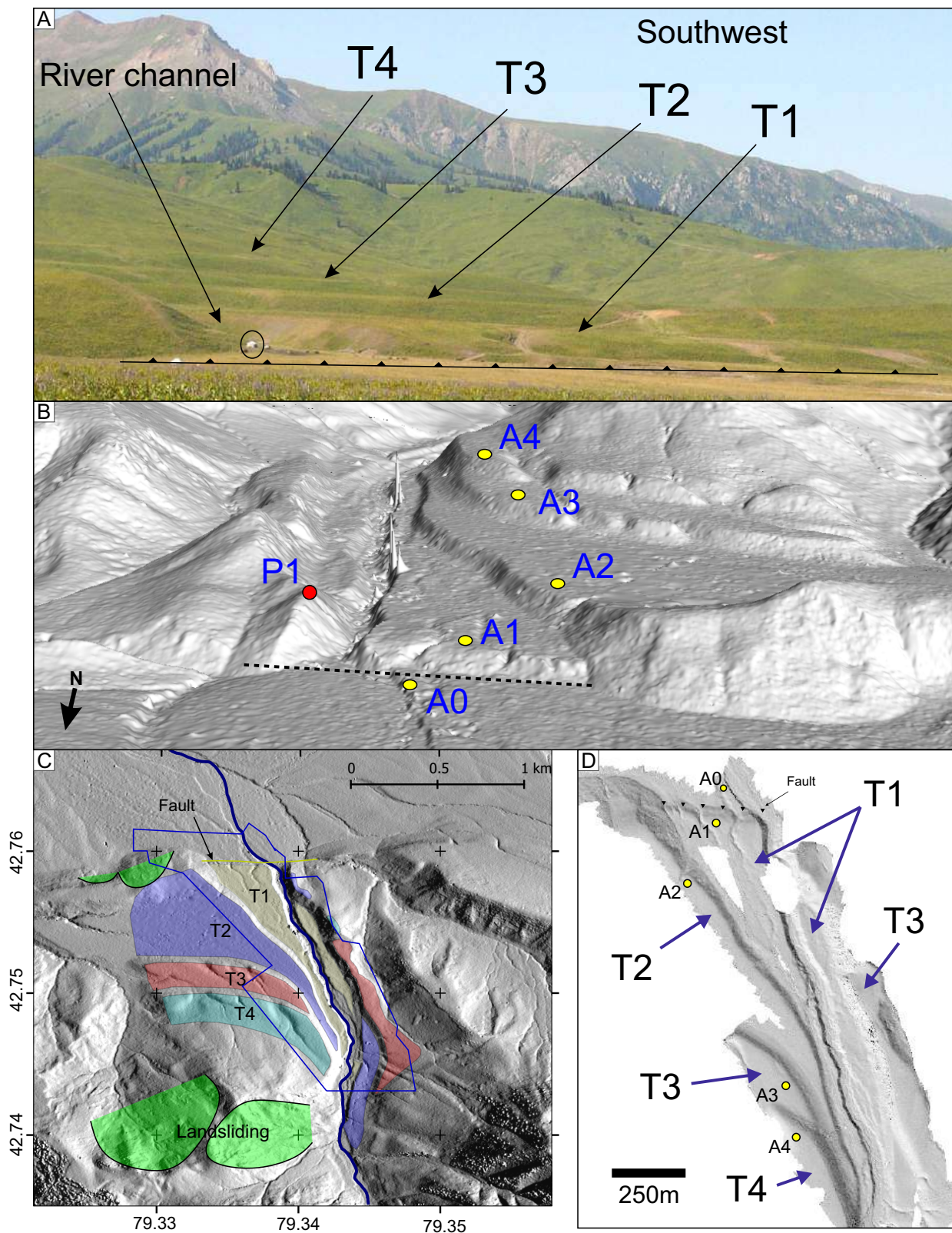


**Figure 3.** (a) Overview of the stepped terraces, T1-4, with the fault in the foreground, yurt circled for scale. (b) Perspective view looking south at the flight of terraces, based on shaded relief of the Pléiades 2 m DEM. Sampling sites are marked as yellow dots. Red dot marks location of photo in Figure 5. 2x vertical exaggeration. (c) Map of the terraces at Rc1. T1-4 shown as coloured polygons with colours consistent with the terraces shown in later figures. Green line marks the fault surface trace in the most recently abandoned terrace. Landslides shown as green polygons. Blue outline shows the extents of the SfM survey in (d). (d) Shaded relief of the 30 cm SfM DEM, with terraces and sampling locations labelled.

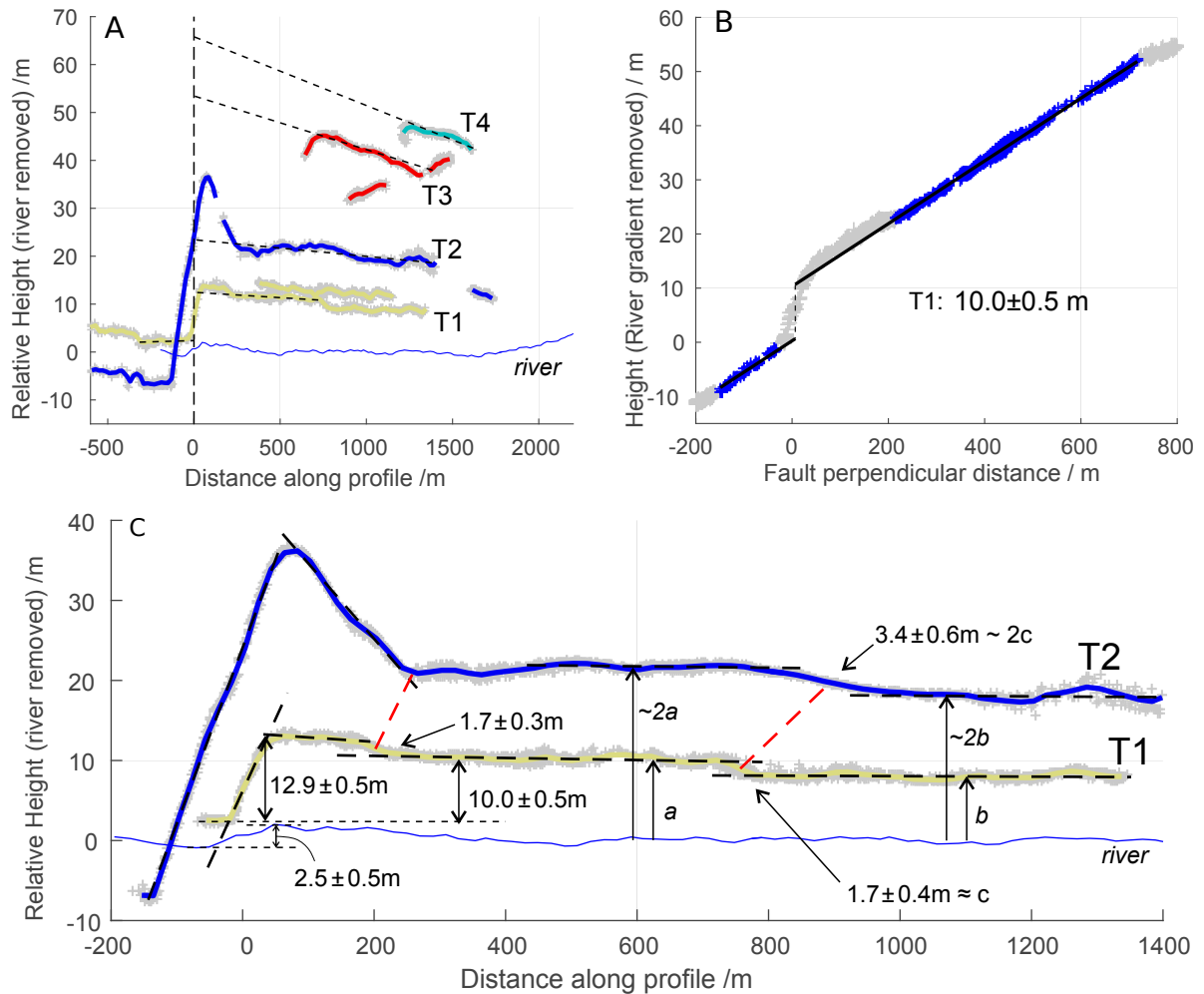


**Figure 4.** (a) Profiles along each of the identified river terraces orthogonal to local fault strike and with the x-axis origin set at the fault. The present river gradient has been removed from all profiles (blue line shows the residual river). Colours correspond to the polygon colours in Figure 3c. (b) Profile across the most recent terrace T1 (without river gradient removed). Offset:  $10.0 \pm 0.5$  m, though this is larger in the  $\sim 200$  m nearest the fault trace. (c) Zoomed section of terraces T1 and T2 in (a). Two steps in the T1 and T2 terrace surfaces are well correlated (dashed red lines), and approximate offsets shown. The steepening of the river gradient near the fault is visible, with an offset of  $\sim 2.5$  m.

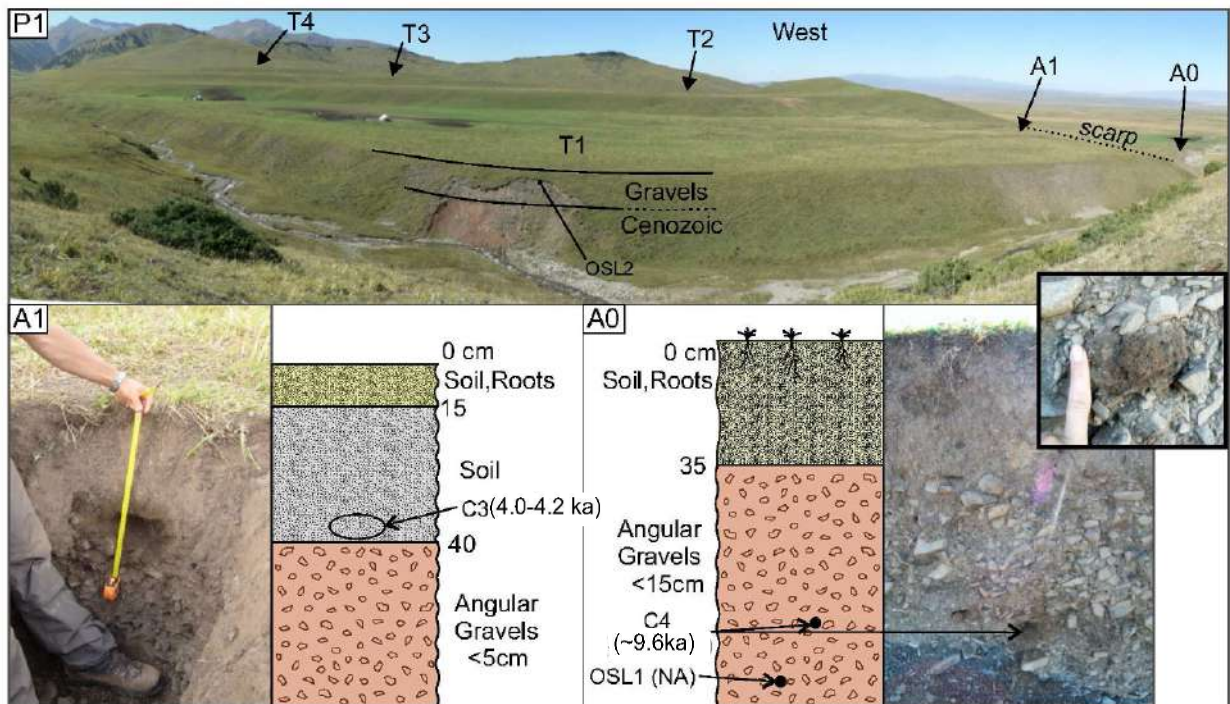


**Figure 5.** (top) Panorama looking across the T1 surface from the opposite side of the river (location in Figure 3). The contact between the red Neogene sediments and the terrace gravels is visible in the terrace riser in the foreground. (A1) Stratigraphy of the Pit in T1 in the hangingwall, ~0.40 m soil, overlying fluvial gravels. (A0) Stratigraphy of the stream cut exposure in the footwall deposits. ~0.45 m Soil thickness, overlying fluvial gravels interspersed with occasional sand lenses. Locations of the radiocarbon and OSL/IRSL samples are shown. Radiocarbon ages are described fully in Table 1.

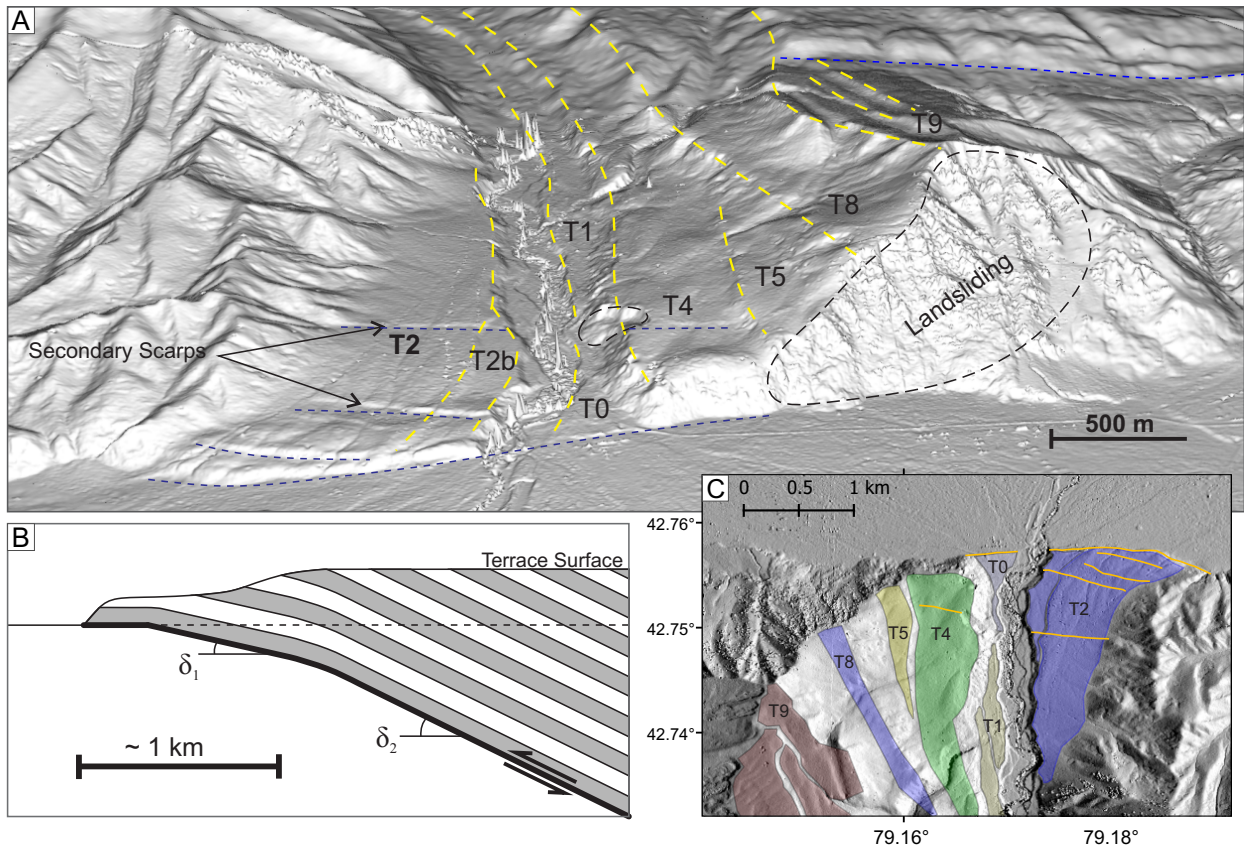


**Figure 6.** (a) Perspective view of the DEM at the border site at Rc2 (looking S, illuminated from viewpoint). The background low resolution DEM is from the AW3D30 dataset, in which the larger terraces are still visible. Terrace riser tops are highlighted with yellow dashed lines. Fault scarps are shown as blue dashed lines. (b) Hypothetical model of the shallow subsurface based on the terrace deformation (see Figure 7) with indicative horizontal scale included. The fault is likely to flatten into a detachment at depths greater than represented here, as inferred from southward-directed tilting of the terraces over distances of greater than 1 km. (c) Map of the terraces observed at Rc2, on top of shaded relief from the Pléiades DEM (illuminated from the East). Terrace polygon colours are consistent with those correlated at the other catchments.

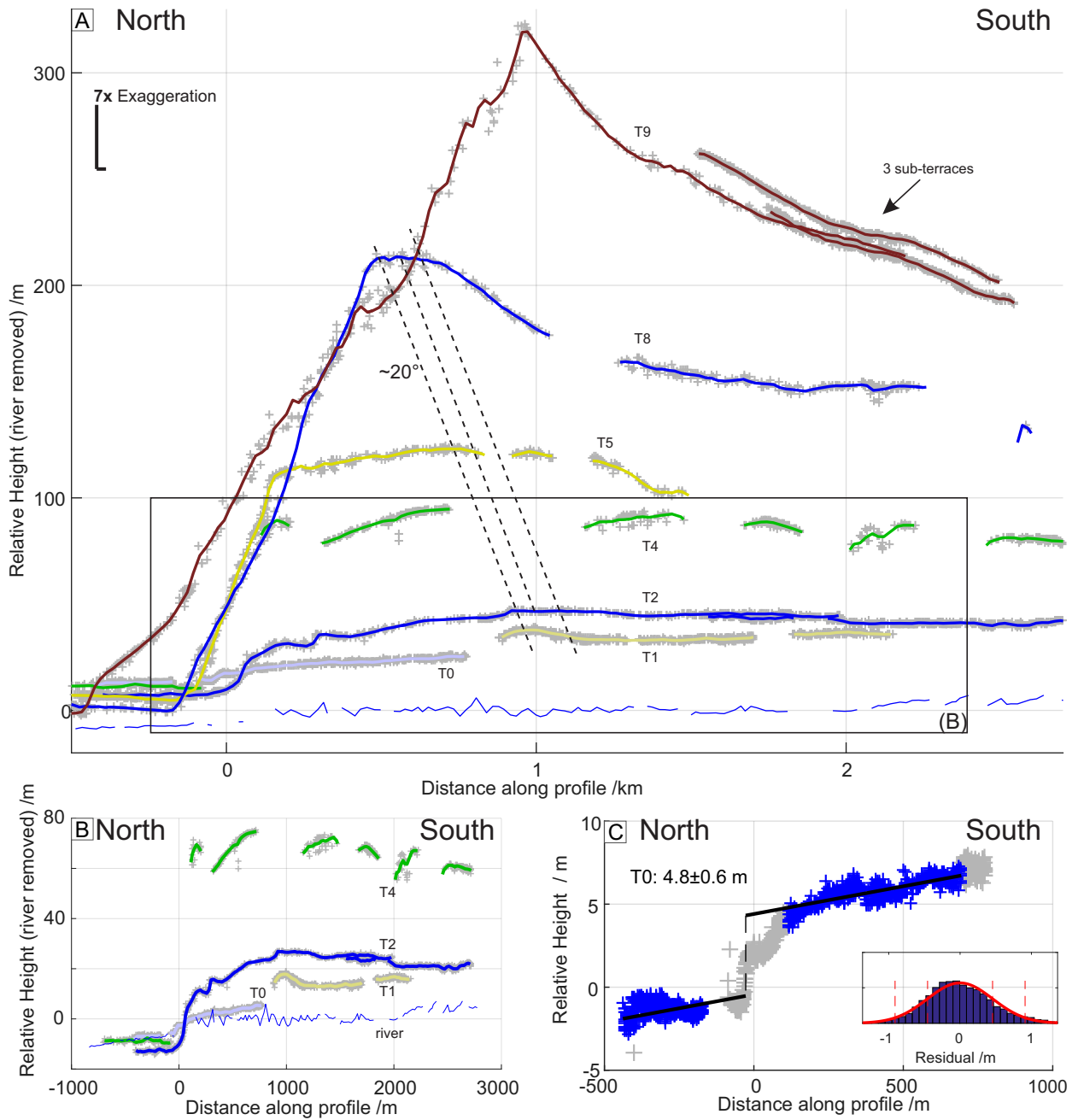


**Figure 7.** (a) Long profiles along all of the terraces, collapsed onto an azimuth of 80°. All of the terraces show an increase in displacement relative to modern river level towards the basin, suggesting the fault dip flattens upwards.(b) Profiles across the lowest four terraces at the Rc2 catchment show a broad warping. It is unclear whether T1 and T0 are the same terrace. (c) Profile across the unique low scarp (T0), measuring a vertical offset of  $\sim 4.8$  m at the fault trace (inset shows histogram of residuals).

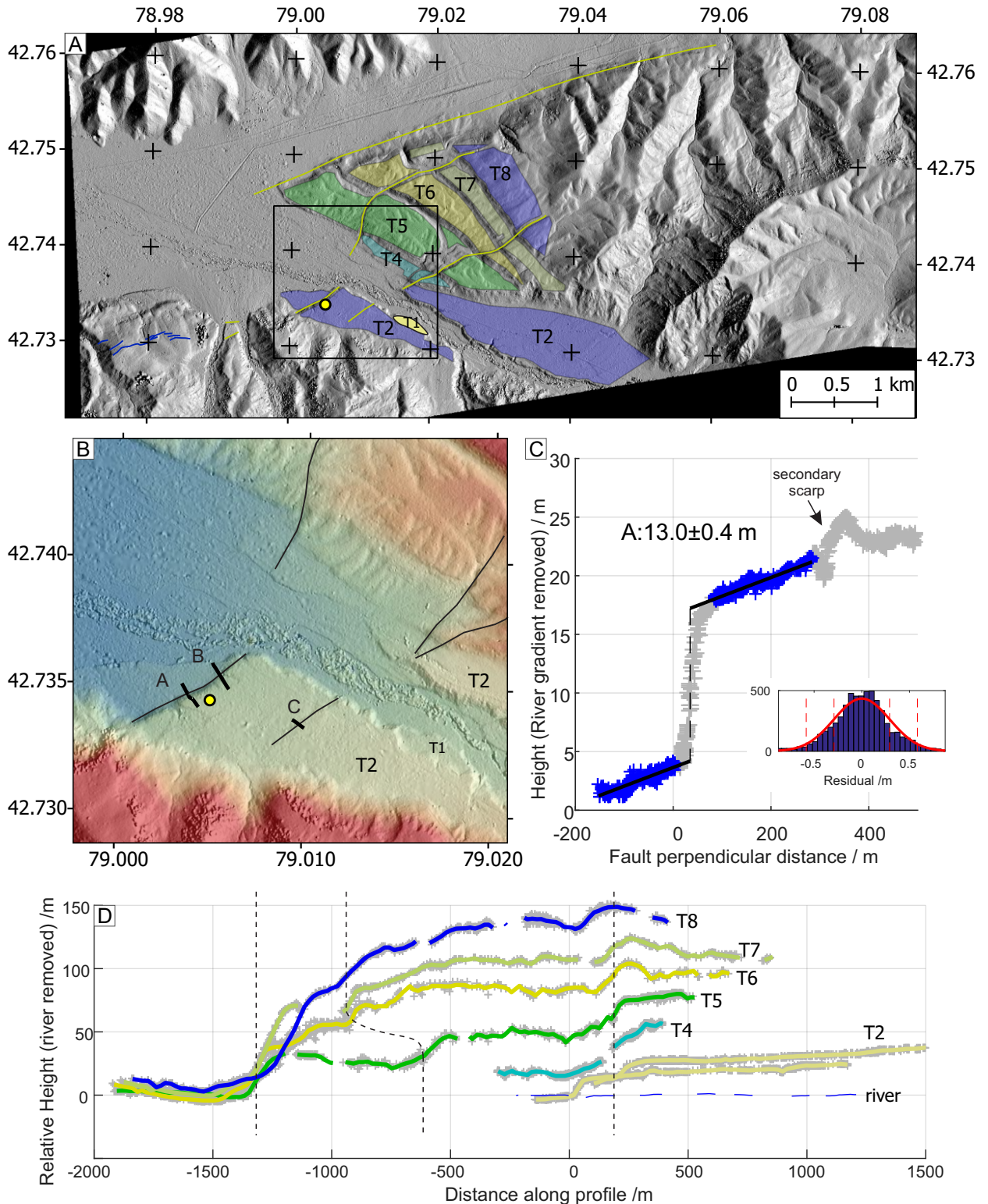


**Figure 8.** (a) Map of the Basharin site, highlighting the series of terraces observed. Labels correspond to the correlated terraces at other sites (§2.2). (b) Zoom near the scarp, showing the location of the three shallow hammer seismic refraction/reflection lines across the scarps, and the sampling pit location. (c) A topographic profile across the scarp in the most recent displaced terrace (T1), in the vicinity of seismic reflection profiles A and B. The inset shows the histogram of residuals. (d) Long profiles through the flight of terraces collapsed onto an azimuth of  $070^\circ$ , show displacements of up to 150 m relative to the modern river channel; the older terraces mark fault displacement in several locations (dashed lines). The older terraces with greater maximum displacement show more displacement further north, while the more recent terrace only shows displacement on the southern fault strand.

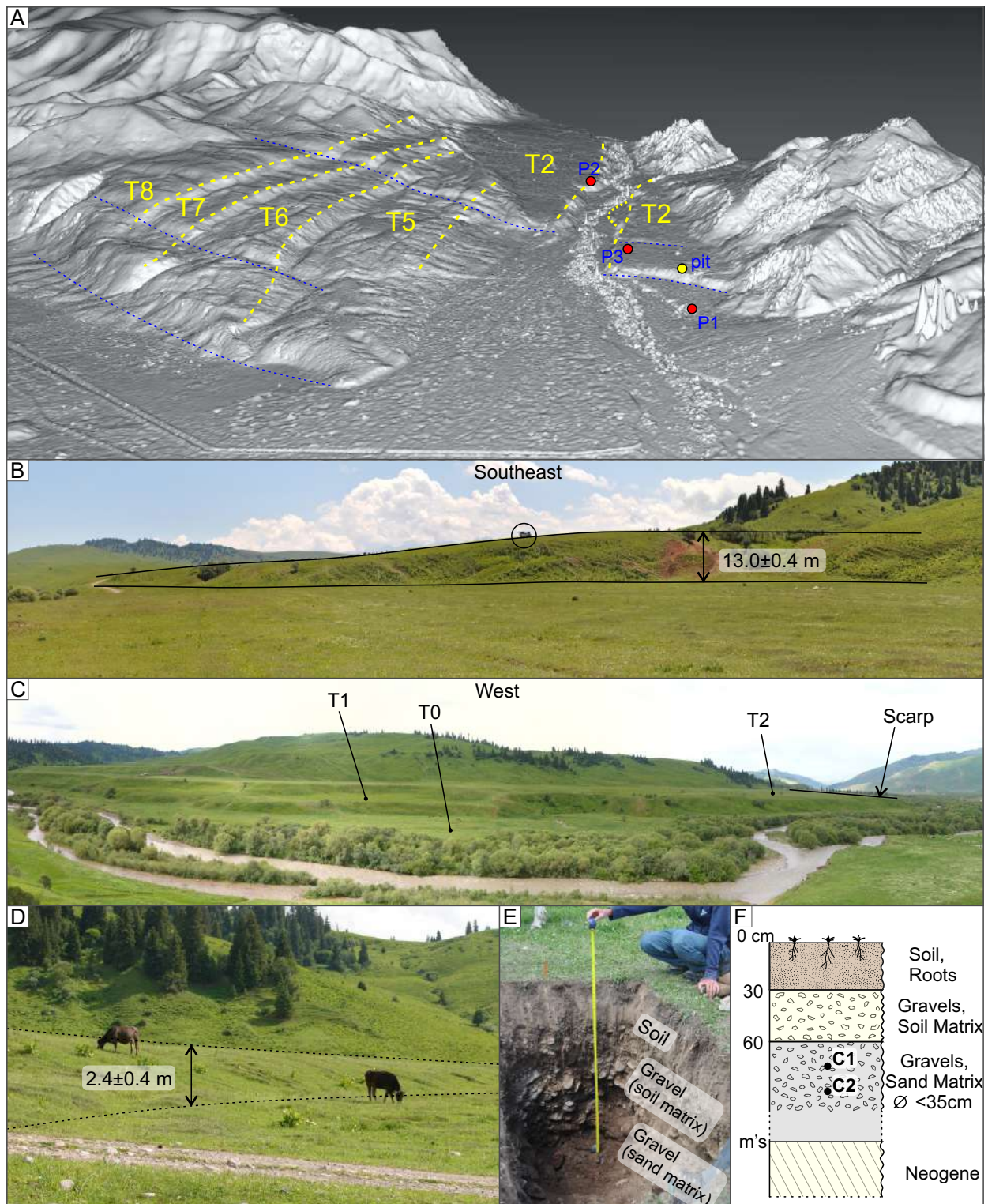


**Figure 9.** (a) Perspective view of the flight of terraces at Rc3. Note the tilting of the terraces away from the river channel. P1, P2 and P3 mark the locations of the photos in (b), (c) and (d) respectively. Blue dashed lines mark fault scarps. (b) Panoramic view (3 photos stitched in cylindrical projection) of the fault scarp in the T2 terrace surface, with an offset of  $\sim 13$  m. Car for scale. (c) Panoramic view of the terraces on the western bank (5 photos, stitched in stereographic projection). (d) The smaller secondary scarp (cows for scale),  $\sim 400$  m from the main scarp in the terrace surface of T2 has an offset of  $\sim 2.4$  m. (e) Sampling pit in the T2 surface. (f) Stratigraphy of the T2 terrace surface. Both radiocarbon samples came from within the gravels with a sand matrix. The presence of Neogene sediments at several metres depth is inferred from outcrops in the present river bed and the seismic reflection profile.

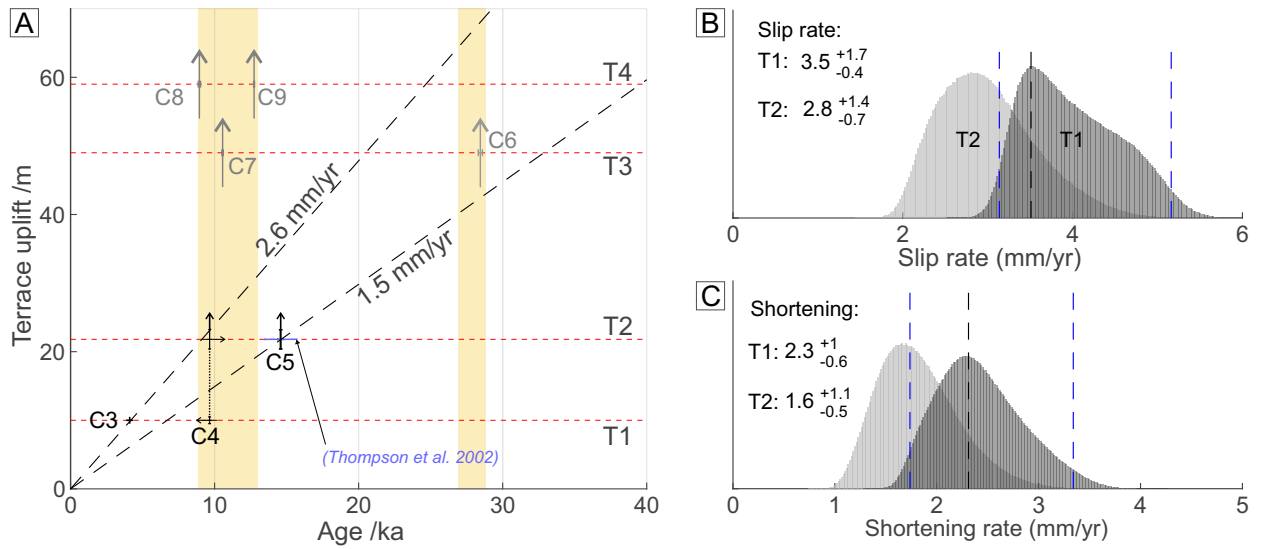


**Figure 10.** (a) Plot of uplift against age for the terraces at Rc1. Points in black represent those used to estimate uplift rates. Grey points represent anomalously young ages, possibly due to accelerated soil development or excessive groundwater in the post-LGM period. Yellow highlight indicates the two short periods that capture the majority of the dated samples. Horizontal dashed lines represent the estimated minimum terrace uplifts relative to the modern river level. (b-c) Monte-Carlo simulation generated PDFs for the shortening rate and slip rate based on the uplift rates for T1 and T2.

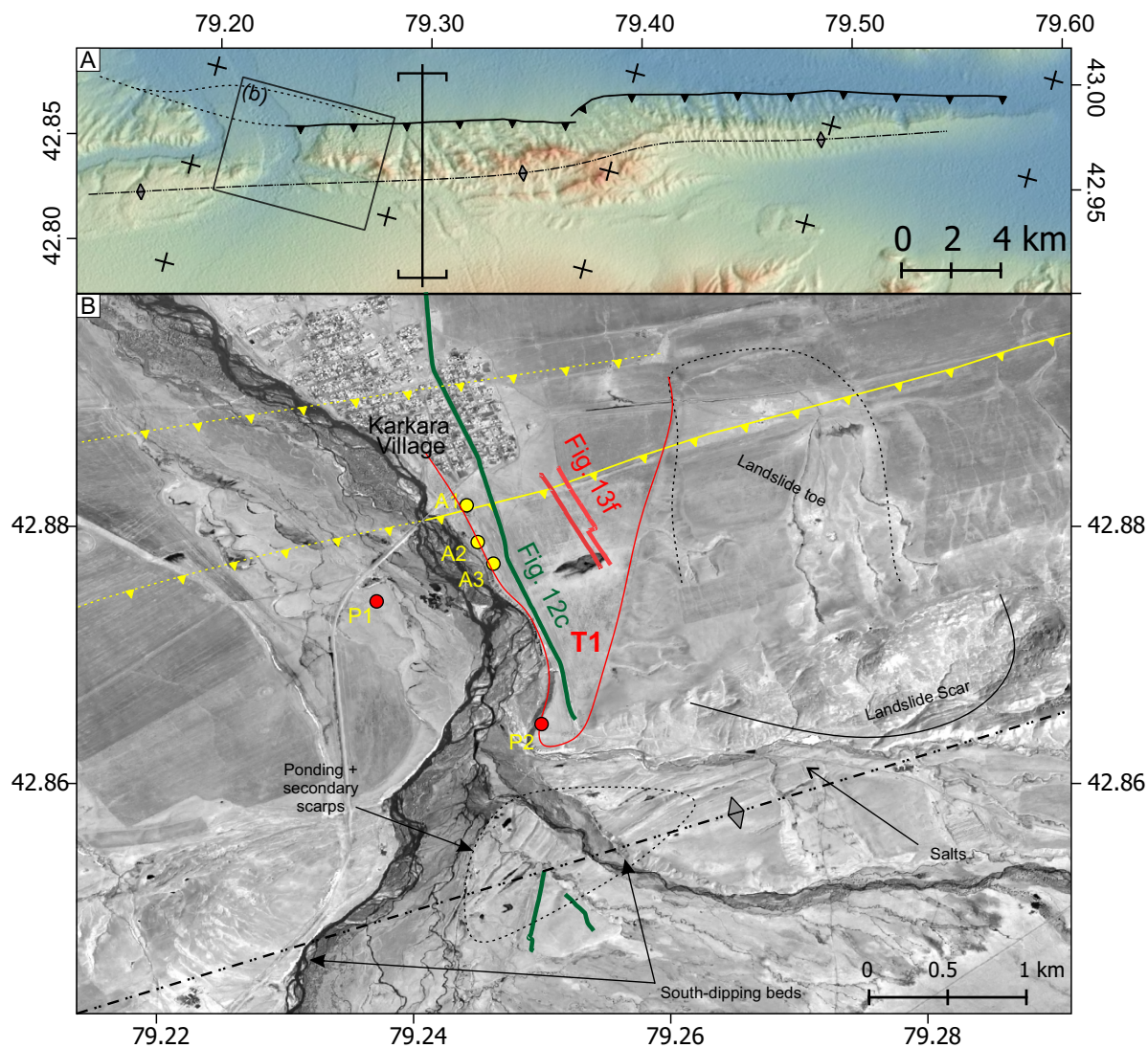


**Figure 11.** (a) Map of the Kegen Basin Fold, which runs approximately NE-SW across the Kegen Basin. The estimated fold axis is shown, along with the mapped fault at the surface along the northern edge of the fold. B–B' marks the location of the topography swath profile in Figure 12 (b) Map of site Q7, where the Karkara River cuts the Kegen fold. Basemap is 1 m resolution panchromatic Kompsat-2 imagery. Locations of the GPS profiles are shown as red and green lines. Sampling sites are shown as yellow dots, and the locations of the photos in Figures 12a,b, 13a, are shown as red dots.

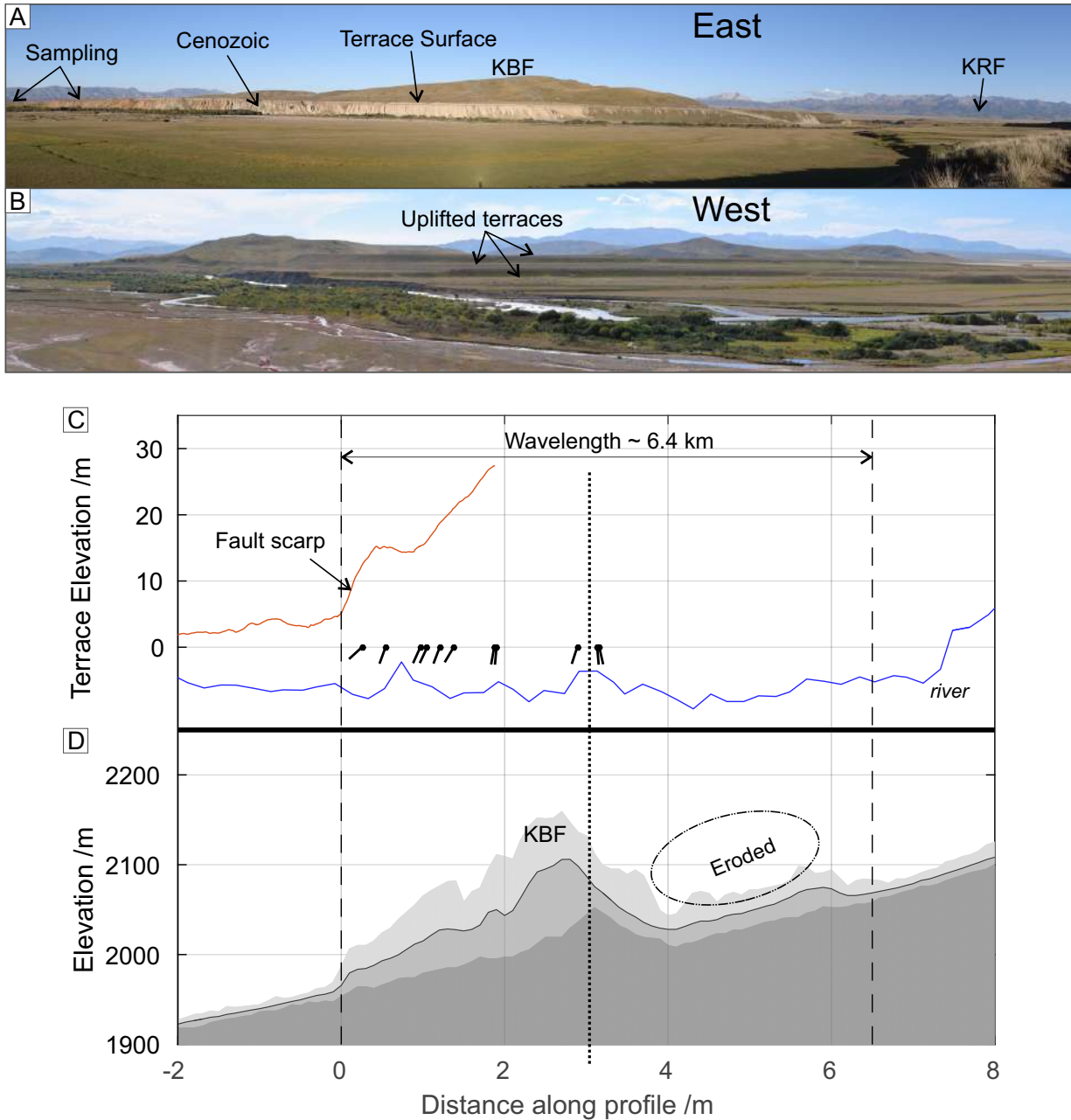


**Figure 12.** (a) Photograph looking east across the Karkara river to the long continuous terrace surface on the eastern side. The terrace consists of a thin gravel layer lying unconformably on steeply dipping Cenozoic sediments. Behind the terrace, the profile of the fold can be seen. (b) Photograph looking west across the Karkara river to the flight of terraces on the western side. (photo locations in Figure 11). (c) Long terrace profile with kinematic GPS along the terrace warped by folding is shown in red. The present river gradient, estimated from SRTM, has been removed from the profiles. The residuals to a linear fit to the present river channel over the wavelength from the fold is shown in blue. The apparent bedding dips are marked in black, showing a clear change from north dipping to south dipping at  $\sim 3$  km from the fault trace (markers not scaled to the vertical axis). (d) Cross section through the minimum, mean and maximum topography across the fold in the swath profile shown in Figure 11.

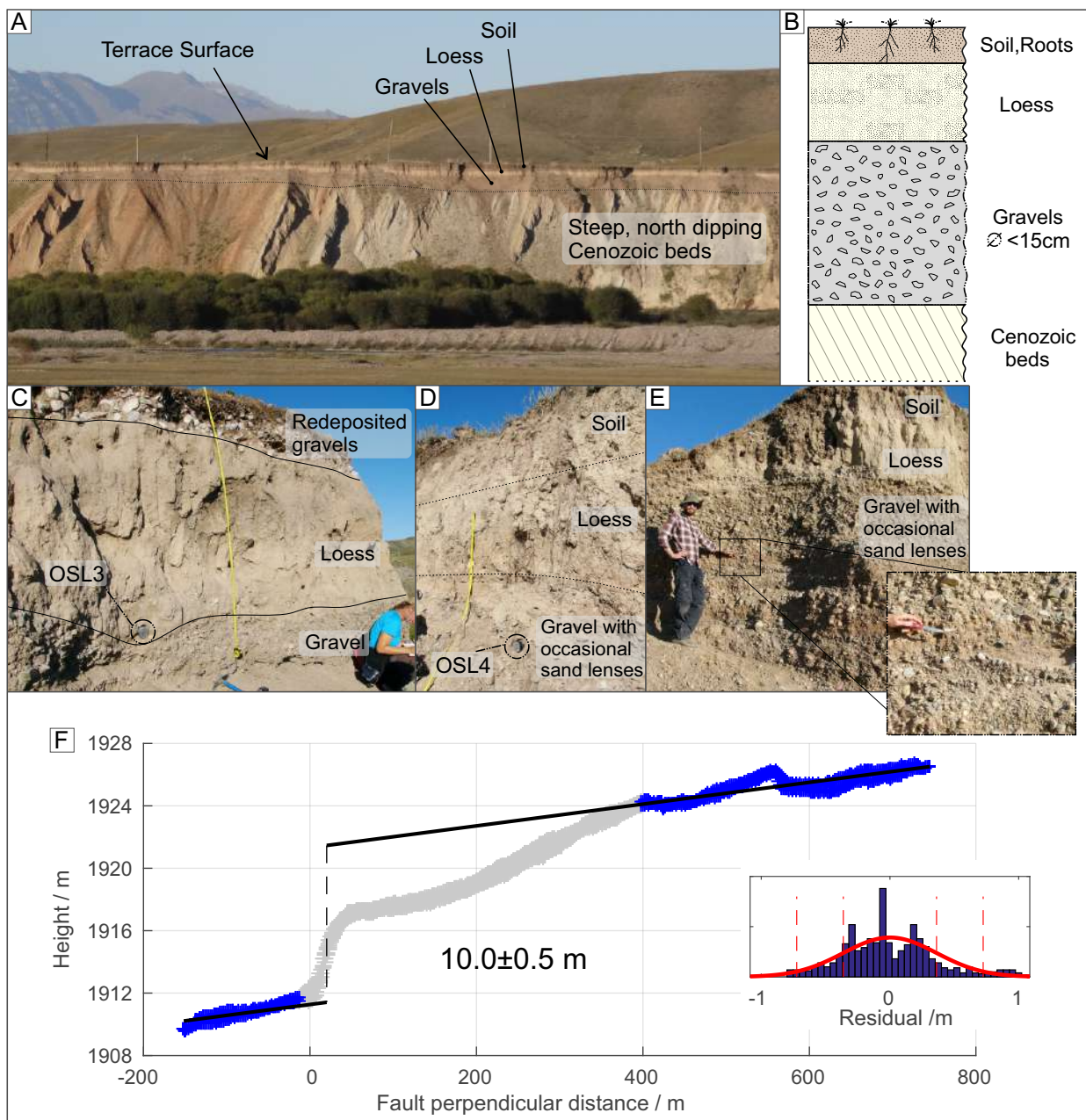


**Figure 13.** (a) View east across the river. Steeply north-dipping Cenozoic sediments are capped with terrace deposits. (b) Approximate profile of the terrace stratigraphy. A thin soil cap sits on top of a thick (1–3 m) loess layer. Beneath this, ~1–5 m of gravels, lie unconformably on the the Cenozoic sediments. (c) Setting of sample OSL1. With an age of 15–17 ka (Tables 2– 3) we interpret this as being within post abandonment channel fill. (d) Sample OSL2, from a coarse sand lens within the terrace gravels. (e) Sample C10, amalgamated gastropod shell fragment sample from a shell containing lens of sand within the terrace gravels. Sample C11 was collected from a similar setting ~500 m further south. (f) Two stacked kinematic GPS profiles across the fault scarp near the town of Karkara show an offset of  $10.0 \pm 0.5$  m in the terrace surface at the fault scarp. The inset shows a histogram of residuals to the linear fit.

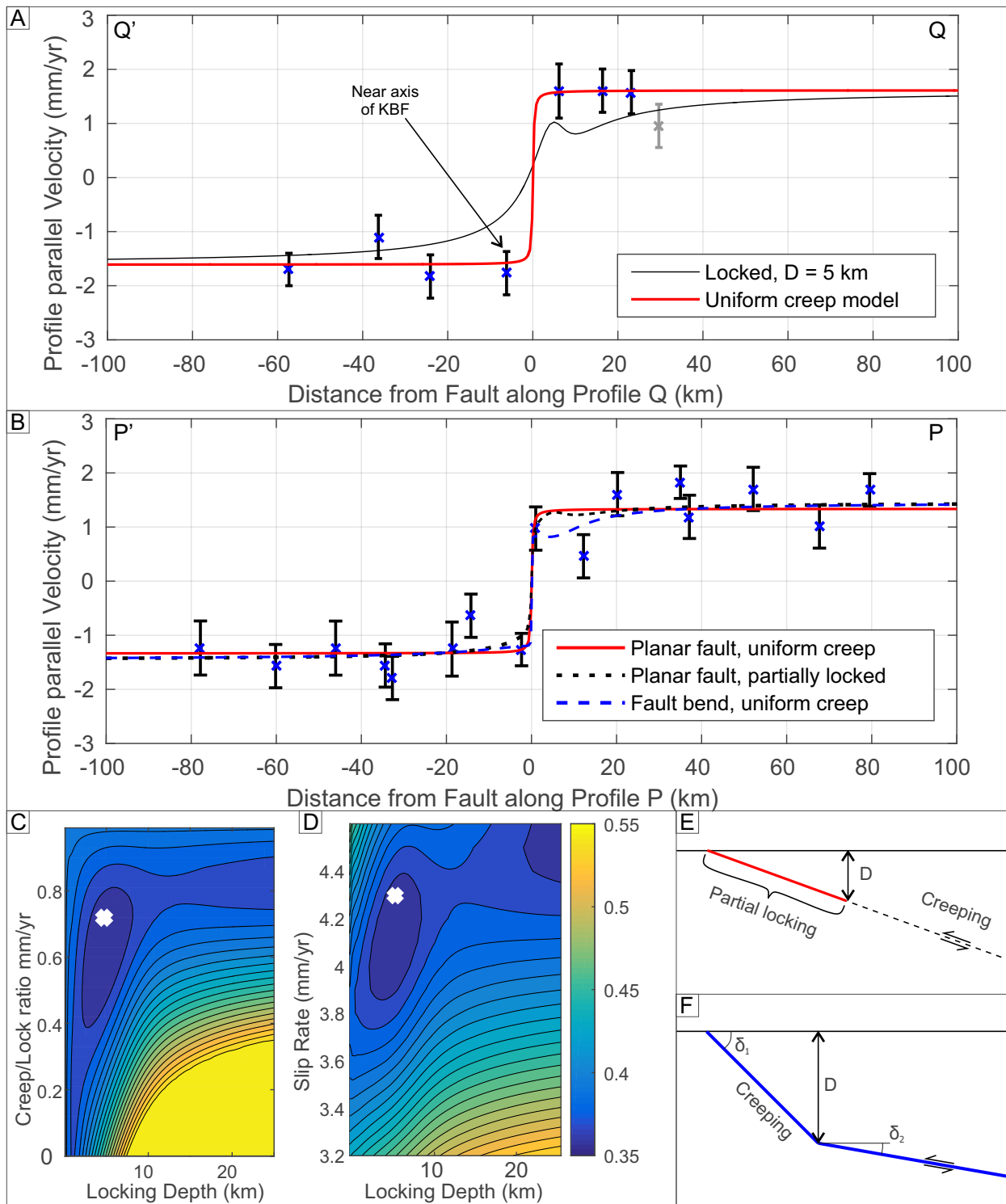


**Figure 14.** (a–b) Modelling of profiles Q and P through the regional GPS field of Zubovich et al. (2010), perpendicular to the KRF. Errorbars indicate the 95% confidence interval. Profile Q is well fit by a single planar fault creeping right to the surface, whereas profile P is better fit either by a partially locked upper segment, or a change in geometry at  $\sim 5$ – $10$  km depth. Map locations of stations shown in Figure 1. (c) Rms well for the locking ratio with locking depth in the partially locked model for profile P. (d) Rms well for the slip-rate with locking depth in the partially locked model for profile P. (e–f) Schematic diagrams of the partially locked model and flat-ramp model giving the fits in (b).

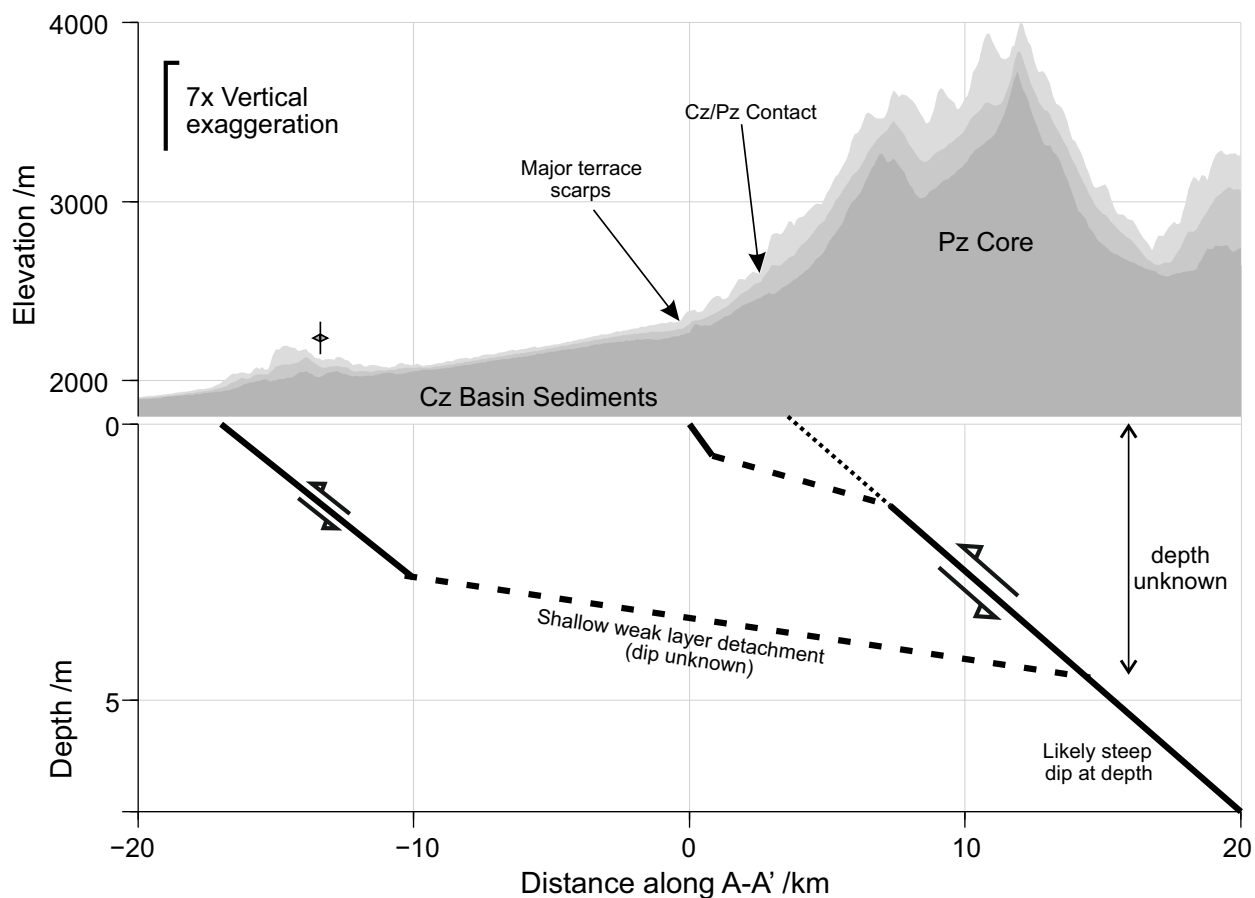


**Figure 15.** Conceptual model of the Karkara Rangefront Fault (KRF) and the Kegen Basin Fold (KBF). The KBF has a width of 6.5 km, suggesting that it is underlain by a ramp that shallows into a detachment at several kilometres depth, and which we interpret to extend southwards to connect with the KRF. The active trace of the KRF is sited north of the Cenozoic-Palaeozoic bedrock contact. The deformation of terraces in the hanging wall of the fault suggest that it shallows into a detachment at only 1-2 km depth, which is also likely to splay from the main fault zone.

| N   | Lab code | Rc  | Material                              | Terrace | Depth (cm) | Delta-13C (o/oo) | Conventional Radiocarbon Age (yr BP) | Calibrated Age (yr BP) |
|-----|----------|-----|---------------------------------------|---------|------------|------------------|--------------------------------------|------------------------|
| C1  | 397882   | Rc3 | Organic rich sediment                 | II      | 86         | -19.3            | 4280±30                              | 4.82–4.96              |
| C2  | 395357   | Rc3 | Organic rich sediment                 | II      | 105        | -10.7            | 22850±90                             | 26.99–27.45            |
| C3  | 397881   | Rc1 | Bulk organic rich soil                | I       | 35–41      | -23.9            | 3750±30                              | 3.99–4.23              |
| C4  | 395371   | Rc1 | Peat/Soil clast                       | I       | 58         | -20.8            | 8710±30                              | 9.55–9.76              |
| C5  | 397880   | Rc1 | Peat/Soil clast                       | II      | 124        | -20.4            | 12440±50                             | 14.22–14.94            |
| C6  | 395348   | Rc1 | Peat/Soil clast                       | III     | 76         | -20.7            | 24400±100                            | 28.2–28.7              |
| C7  | 395350   | Rc1 | Peat/Soil clast                       | III     | 88         | -21.7            | 9340±30                              | 10.44–10.66            |
| C8  | 397883   | Rc1 | Bulk organic rich soil                | IV      | 67         | -21.8            | 8050±30                              | 8.78–9.03              |
| C9  | 404173   | Rc1 | Bulk clay                             | IV      | 80         | -22.8            | 10860±40                             | 12.69–12.80            |
| C10 | 35584*   | Q7  | Amalgamated gastropod shell fragments | –       | 150        | -6.3             | 32230±190                            | 35.7–36.5              |
| C11 | 35585*   | Q7  | Amalgamated gastropod shell fragments | –       | 160        | -8.6             | 34110±210                            | 38.2–39.1              |

**Table 1.** Full description of the Radiocarbon ages obtained at each of the sites studied along the Karkara Rangefront. Rc1–3: Karkara Rangefront, Q7: Kegen Basin Fold. Ages are reported as radiocarbon years before present where present = AD 1950. Sample analysis was performed by Beta Analytics except for those marked \* which were analysed at the Oxford Radiocarbon Accelerator Unit (ORAU). Ages calibrated based on the IntCal13 atmospheric curve (Reimer 2013), using the OxCal utility (Bronk Ramsey 2009). Errors on the radiocarbon age are 1- $\sigma$  analytical uncertainties. The calibrated age range presented is the 95% confidence interval based on the analytical uncertainty and the uncertainty in the calibration curve.

| Name | Site | Depth (cm) | Material    | Water (%) | Feldspar grain size ( $\mu\text{m}$ ) | Feldspar total dose rate ( $\text{Gy ka}^{-1}$ ) | Feldspar CAM $D_e$ pIRIR <sub>255</sub> ( $\text{Gy}$ ) | Aliquots n <sub>255</sub> | OD (%) | Uncorrected IRSL 50°C Age (ka) | Fading corrected IRSL 50°C age (ka) | pIRIR <sub>225</sub> Age (ka) | pIRIR <sub>290</sub> Age (ka) |
|------|------|------------|-------------|-----------|---------------------------------------|--|---|---------------------------|--------|--------------------------------|-------------------------------------|-------------------------------|-------------------------------|
| OSL1 | Rc1  | 70         | sand        | 3.2±3     | 180-250                               | 5.89±0.23  | 106±6 <sup>a</sup>                                      | 21                        | 20     | 9.0±0.5                        | 15.5±1.5                            | 18.0±1.2                      | —                             |
| OSL2 | Rc1  | 75         | sand        | 7.8±3     | 180-250                               | 5.37±0.21  | 127±9 <sup>b</sup>                                      | 18                        | 26     | 11.6±0.7                       | 22.3±3.6                            | 23.7±1.9                      | —                             |
| OSL3 | S7   | 180        | loess/silt  | 1.1±3     | 180-212                               | 4.43±0.18  | 74±3  | 16                        | 9      | 14.4±0.8                       | 17.1±0.9                            | 16.6±0.9                      | 17.4±1.0                      |
| OSL4 | S7   | 215        | coarse sand | 0.8±3     | 180-212                               | 4.21±0.17  | 139±7 <sup>c</sup>                                      | 15                        | 13     | 27.0±1.8                       | 33.0±2.2                            | 33.0±2.1                      | 40.2±3.1                      |

<sup>a</sup> One high outlier removed

<sup>b</sup> Two high outliers removed

<sup>c</sup> One high and one low outlier removed

**Table 2.** Feldspar pIRIR ages for the luminescence samples, labels are consistent with those for the same samples analysed for quartz OSL. Samples OSL1 and OSL2 showed large overdispersion, generally dim signals and exhibits a significant residual dose after bleaching, suggesting incomplete bleaching may have occurred prior to deposition – they are not used in calculating slip rates. Errors represent 1- $\sigma$  uncertainties.

| Name | Site | Depth (cm) | Material    | Water (%) | Grain size ( $\mu\text{m}$ ) | Total dose rate ( $\text{Gy ka}^{-1}$ ) | Palaeodose $D_e$ ( $\text{Gy}$ ) | Aliquots | OD (%) | Quartz age (ka) |
|------|------|------------|-------------|-----------|------------------------------|---|----------------------------------|----------|--------|-----------------|
| OSL3 | S7   | 180        | loess/sand  | 1.1±3     | 180-250                      | 3.55±0.16                               | 53.8±2.8                         | 18       | 15.1   | 15.2±1.1        |
| OSL4 | S7   | 215        | coarse sand | 0.8±3     | 212-250                      | 3.33±0.16                               | 75.3±3.2                         | 24       | 12.6   | 22.6±1.4        |

**Table 3.** Quartz OSL dates for the OSL3–4 samples from the folded terrace at Kegen. OSL3 is believed to be loess fill in a channel cut into the terrace surface, giving a post-date on terrace abandonment. OSL4 was coarser sand material, yields a quartz age significantly younger than the pIRIR age for the same sample and the <sup>14</sup>C estimates. Errors represent 1- $\sigma$  uncertainties.

889 This paper has been produced using the Blackwell Scientific Publications GJI L<sup>A</sup>T<sub>E</sub>X2e class file.